A&A 608, A89 (2017)
DOI: 10.1051/0004-6361/201731582

Astronomy & Astrophysics

The formation of the Milky Way halo and its dwarf satellites; a NLTE-1D abundance analysis

II. Early chemical enrichment*

L. Mashonkina[1,2], P. Jablonka[3,4], T. Sitnova[2], Yu. Pakhomov[2], and P. North[3]

[1] Universitäts-Sternwarte München, Scheinerstr. 1, 81679 München, Germany
e-mail: lyuda@usm.lmu.de
[2] Institute of Astronomy, Russian Academy of Sciences, 119017 Moscow, Russia
e-mail: lima@inasan.ru
[3] Laboratoire d'Astrophysique, École Polytechnique Fédérale de Lausanne (EPFL), Observatoire de Sauverny, 1290 Versoix, Switzerland
[4] GEPI, Observatoire de Paris, CNRS, Université Paris Diderot, 92125 Meudon Cedex, France

Received 17 July 2017 / Accepted 14 September 2017

ABSTRACT

We present the non-local thermodynamic equilibrium (NLTE) abundances of up to 10 chemical species in a sample of 59 very metal-poor (VMP, $-4 \leq$ [Fe/H] $\lesssim -2$) stars in seven dwarf spheroidal galaxies (dSphs) and in the Milky Way (MW) halo. Our results are based on high-resolution spectroscopic datasets and homogeneous and accurate atmospheric parameters determined in Paper I. We show that once the NLTE effects are properly taken into account, all massive galaxies in our sample, that is, the MW halo and the classical dSphs Sculptor, Ursa Minor, Sextans, and Fornax, reveal a similar plateau at [α/Fe] $\simeq 0.3$ for each of the α-process elements: Mg, Ca, and Ti. We put on a firm ground the evidence for a decline in α/Fe with increasing metallicity in the Boötes I ultra-faint dwarf galaxy (UFD), that is most probably due to the ejecta of type Ia supernovae. For Na/Fe, Na/Mg, and Al/Mg, the MW halo and all dSphs reveal indistinguishable trends with metallicity, suggesting that the processes of Na and Al synthesis are identical in all systems, independent of their mass. The dichotomy in the [Sr/Ba] versus [Ba/H] diagram is observed in the classical dSphs, similarly to the MW halo, calling for two different nucleosynthesis channels for Sr. We show that Sr in the massive galaxies is well correlated with Mg suggesting a strong link to massive stars and that its origin is essentially independent of Ba, for most of the [Ba/H] range. Our three UFDs, that is Boötes I, UMa II, and Leo IV, are depleted in Sr and Ba relative to Fe and Mg, with very similar ratios of [Sr/Mg] $\simeq -1.3$ and [Ba/Mg] $\simeq -1$ on the entire range of their Mg abundances. The subsolar Sr/Ba ratios of Boötes I and UMa II indicate a common r-process origin of their neutron-capture elements. Sculptor remains the classical dSph, in which the evidence for inhomogeneous mixing in the early evolution stage, at [Fe/H] < -2, is the strongest.

Key words. line: formation – nuclear reactions, nucleosynthesis, abundances – stars: abundances – stars: atmospheres – galaxies: abundances – galaxies: dwarf

1. Introduction

We aim at understanding the physical conditions at the onset of star formation in galaxies. The stellar abundance trends and dispersions of the most metal-poor stars reveal the nature of the first generations of stars, that is, their masses, numbers, and spatial distribution, the nature and energetics of the explosion of supernovae, and the level of homogeneity of the primitive interstellar medium (e.g. sizes and masses of star forming regions). The proximity of the Local Group dwarf spheroidal galaxies (dSphs) allows the derivation of chemical abundances with comparable quality as in the Milky Way (MW). The comparison of these galaxies with very different masses, star formation histories, and level of chemical enrichment can provide crucial information regarding the universality of the physical processes at play. This type of comparative analysis is at the frontier between stellar and galaxy evolution. For example, such an analysis provides a very detailed testbed for the Λ cold dark matter paradigm and improves our understanding of fundamental parameters, such as the sampling of the initial mass function. This research also provides the most necessary constraints on the nucleosynthetic origin of still puzzling categories of chemical species, such as the neutron-capture elements or the odd-nuclear charge (odd-Z) elements sodium and aluminum.

As a consequence of their distance, most of the stars accessible in dSphs at high spectral resolution are giants. Low total gas pressure and low electron number density lead to departures from local thermodynamical equilibrium (LTE) in their atmospheres, while the non-local thermodynamical equilibrium (NLTE) line formation impacts each chemical species differently, in magnitude and sign, depending on the stellar atmosphere parameters and element abundances (for review, see Asplund 2005; Mashonkina 2014). Therefore, ignoring the NLTE effects for stellar samples covering broad metallicity ranges can lead to a distorted picture of the galactic abundance trends.

* Full Tables 3 and 4 are only available at the CDS via anonymous ftp to cdsarc.u-strasbg.fr (130.79.128.5) or via http://cdsarc.u-strasbg.fr/viz-bin/qcat?J/A+A/608/A89

This paper is the second part of a project aiming at providing a homogeneous set of NLTE elemental abundances for the very and extremely metal-poor (VMP: [Fe/H][1] ≤ -2, EMP: [Fe/H] ≤ -3) stars both in the Local Group dwarf spheroidal galaxies and in the halo of the Milky Way. Accurate atmospheric parameters for our stellar sample were derived in our previous study (Mashonkina et al. 2017, hereafter Paper I).

Our work has been preceded by a number of important efforts to evaluate the NLTE effects on determination of chemical abundances for late-type stars.

In regards to the chemical species of our interest in the metallicity range similar to that of our study, from extremely to very metal-poor stars, the NLTE abundance corrections were calculated for Na I (Baumueller et al. 1998; Mashonkina et al. 2000; Andrievsky et al. 2007), Mg I (Idiart & Thévenin 2000; Shimanskaya et al. 2000; Zhao & Gehren 2000, 2010; Andrievsky et al. 2010) Al I (Baumueller & Gehren 1997; Andrievsky et al. 2008), Si I (Shi et al. 2009), Ca I (Idiart & Thévenin 2000; Mashonkina et al. 2007; Spite et al. 2012), Ti I-Ti II (Bergemann 2011; Sitnova 2016), Sr II (Mashonkina & Gehren 2001; Andrievsky et al. 2011; Bergemann et al. 2012), and Ba II (Mashonkina et al. 1999; Andrievsky et al. 2009). Recently, Zhao et al. (2016) derived the NLTE abundances of a wealth of elements, from Li to Eu, for a sample of 51 Galactic dwarf stars covering the $-2.6 \leq$ [Fe/H] ≤ 0.2 range. The methods used by Zhao et al. (2016) are closest to the present study and are complementary in the spectral type of stars and the metallicity range.

Since in most cases, the departures from LTE for individual lines depend strongly on the stellar atmosphere parameters and elemental abundances, we do not use pre-existing NLTE abundance corrections from the literature. Instead, the NLTE calculations are performed for each star and chemical species. Our approach stands out among the previous publications by three specific features at least: i) we calculate the [X/Fe] abundance ratios by correcting the iron abundances from NLTE effects as well, unlike most of our predecessors; ii) we calculate the NLTE abundances in idem homogeneous way for all elements; and iii) we go beyond the Milky Way stellar population and address the chemical trends of the Local Group dwarf spheroidal galaxies.

In the following, Sect. 2 briefly describes our stellar sample, the observational material, and the adopted method to derive the atmospheric parameters. Details of the NLTE calculations and the abundance determinations, including atomic models, line list, and codes, are provided in Sect. 3. Section 4 details the impact of the NLTE treatment on each individual chemical species, while Sect. 5 presents the abundance trends within each galaxy and draws comparisons between these trends to infer their chemical evolution. It also provides new constrains on the nucleosynthetic origin of the neutron-capture elements. Our results are summarised in Sect. 6.

2. Stellar sample, observational material, and atmospheric parameters

Our stellar sample, the observational material, and the determination of atmospheric parameters were described in Paper I. We summarise below the main features.

Sample. We are working with two stellar samples of cool giants in the $-4 \lesssim$ [Fe/H] $\lesssim -2$ metallicity range. One is composed of 23 stars in the Milky Way halo, the other encompasses 36 stars in a number of MW satellites as follows: the classical dSphs Sculptor (Scl), Ursa Minor (UMi), Fornax (Fnx), and Sextans (Sex), and the ultra-faint dwarfs (UFDs) Boötes I, UMa II, and Leo IV.

Material. Each star was observed at high spectral resolution, $R = \lambda/\Delta\lambda \geq 25\,000$. We used the stellar spectra from public and private archives as well as published equivalent widths.

Stellar atmosphere parameters. We used a combination of photometric and spectroscopic methods to derive a homogeneous set of stellar atmosphere parameters: effective temperature $T_{\rm eff}$, surface gravity log g, iron abundance [Fe/H], and microturbulence velocity $\xi_{\rm t}$. Our spectroscopic analyses take advantage of NLTE line formation.

For both stellar samples we rely on photometric effective temperatures. The surface gravities of the dSph stars were calculated by applying the standard relation between log g, $T_{\rm eff}$, the absolute bolometric magnitude, and the stellar mass, which was assumed to be 0.8 $M_{\odot}$. The Fe I- and Fe II-based NLTE abundances of the dSph stars are fully consistent in the [Fe/H] > -3.7 regime. We therefore applied the Fe I/Fe II ionisation equilibrium method to determine the surface gravities of the MW giants, for which distances are mostly unknown or inaccurate. The abundance difference between Fe I and Fe II does not exceed 0.12 dex and 0.06 dex for the dSph and MW stars, respectively.

The NLTE treatment fails to achieve consistent abundances from Fe I and Fe II in the most metal-poor ([Fe/H] < -3.7) stars in the dSphs. As a consequence, we did not enforce the Fe I/Fe II ionisation equilibrium for the most metal-poor star in the MW comparison sample, HE1357-0123 ([Fe/H] $\simeq -3.9$), but used an upward revised, by 0.2 dex, log g derived by Cohen et al. (2013) from the isochrone method.

The problem of the Fe I/Fe II ionisation equilibrium of our most metal-poor stars most probably relates to the uncertainty in the photometric calibration of $T_{\rm eff}$ at these extremely low metallicities. Hence, our final [Fe/H] values, for the entire sample, are based on lines of Fe II only.

Our sample stars and their atmospheric parameters are listed in Table 1.

3. Method

3.1. NLTE calculations

The present investigation is based on the NLTE methods developed in our earlier studies and documented in a number of papers (see Table 2 for the references), in which the atomic data and questions of line formation were considered in detail. We updated collisional data for a number of chemical species. We apply here the electron-impact excitation rate coefficients from *ab initio* calculations of Bautista et al. (2002) for Sr II. The inelastic collisions with neutral hydrogen particles are treated, for Al I, Si I, and Ca I, using the accurate rate coefficients from quantum-mechanical calculations of Belyaev (2013), Belyaev et al. (2014, and 2016), respectively. For Ti I-II, Fe I-II, Sr II, and Ba II we rely on the Drawin (1968) approximation, as implemented by Steenbock & Holweger (1984), and apply a scaling factor $S_{\rm H}$ to the Drawinian rates. The magnitude of $S_{\rm H}$ indicated in Table 2 is estimated empirically for every chemical species in our earlier papers.

To solve the coupled radiative transfer and statistical equilibrium (SE) equations, we employed a revised version of the DETAIL code (Butler & Giddings 1985) based on the accelerated lambda iteration method, as described in

[1] In the classical notation, where [X/H] = $\log(N_{\rm X}/N_{\rm H})_{\rm star} - \log(N_{\rm X}/N_{\rm H})_{\rm Sun}$.

Table 1. Atmospheric parameters of the investigated sample.

ID	$T_{\rm eff}$ [K]	log g	[Fe/H]	$\xi_{\rm t}$ [km s^{-1}]
Scl ET0381	4570	1.17	−2.19	1.7
Scl002_06	4390	0.68	−3.11	2.3
Scl03_059	4530	1.08	−2.88	1.9
Scl031_11	4670	1.13	−3.69	2.0
Scl074_02	4680	1.23	−3.06	2.0
Scl07-49	4630	1.28	−2.99	2.0
Scl07-50	4800	1.56	−4.00	2.2
Scl11_1_4296	4810	1.76	−3.70	1.9
Scl6_6_402	4890	1.78	−3.66	1.8
Scl S1020549	4650	1.35	−3.67	2.0
Scl1019417	4280	0.50	−2.48	2.0
Fnx05-42	4350	0.70	−3.37	2.3
Sex11-04	4380	0.57	−2.60	2.2
Sex24-72	4400	0.76	−2.84	2.2
UMi396	4320	0.70	−2.26	2.5
UMi446	4600	1.37	−2.52	2.5
UMi718	4630	1.13	−2.00	2.0
UMi COS233	4370	0.77	−2.23	2.0
UMi JI19	4530	1.00	−3.02	2.0
UMi20103	4780	1.55	−3.09	2.0
UMi28104	4275	0.65	−2.12	2.0
UMi33533	4430	0.75	−3.14	2.0
UMi36886	4400	0.82	−2.56	2.0
UMi41065	4350	0.63	−2.48	2.0
Boo-033	4730	1.4	−2.26	2.3
Boo-041	4750	1.6	−1.54	2.0
Boo-094	4570	1.01	−2.69	2.2
Boo-117	4700	1.4	−2.09	2.3
Boo-127	4670	1.4	−1.93	2.3
Boo-130	4730	1.4	−2.20	2.3
Boo-980	4760	1.8	−2.94	1.8
Boo-1137	4700	1.39	−3.76	1.9
UMa II-S1	4850	2.05	−2.96	1.8
UMa II-S2	4780	1.83	−2.94	2.0
UMa II-S3	4560	1.34	−2.26	1.8
Leo IV-S1	4530	1.09	−2.58	2.2
HD 2796	4880	1.55	−2.32	1.8
HD 4306	4960	2.18	−2.74	1.3
HD 8724	4560	1.29	−1.76	1.5
HD 108317	5270	2.96	−2.18	1.2
HD 122563	4600	1.32	−2.63	1.7
HD 128279	5200	3.00	−2.19	1.1
HD 218857	5060	2.53	−1.92	1.4
HE0011-0035	4950	2.0	−3.04	2.0
HE0039-4154	4780	1.6	−3.26	2.0
HE0048-0611	5180	2.7	−2.69	1.7
HE0122-1616	5200	2.65	−2.85	1.8
HE0332-1007	4750	1.5	−2.89	2.0
HE0445-2339	5165	2.2	−2.76	1.9
HE1356-0622	4945	2.0	−3.45	2.0
HE1357-0123	4600	1.2	−3.92	2.1
HE1416-1032	5000	2.0	−3.23	2.1
HE2244-2116	5230	2.8	−2.40	1.7
HE2249-1704	4590	1.2	−2.94	2.0
HE2252-4225	4750	1.55	−2.76	1.9
HE2327-5642	5050	2.20	−2.92	1.7
BD −11° 0145	4900	1.73	−2.18	1.8
CD −24° 1782	5140	2.62	−2.72	1.2
BS16550-087	4750	1.5	−3.33	2.0

Table 2. Atomic models used in this study.

Species	Reference	H I collisions
Na I	Alexeeva et al. (2014)	BBD10
Mg I	Mashonkina (2013)	BBS12
Al I	Baumueller & Gehren (1996)	B13
Si I	Shi et al. (2008)	BYB14
Ca I-II	Mashonkina et al. (2007)	BYG16
Ti I-II	Sitnova et al. (2016)	$S_{\rm H}$ = 1
Fe I-II	Mashonkina et al. (2011)	$S_{\rm H}$ = 0.5
Sr II	Belyakova & Mashonkina (1997)	$S_{\rm H}$ = 0.01
Ba II	Mashonkina et al. (1999)	$S_{\rm H}$ = 0.01
Eu II	Mashonkina & Gehren (2000)	$S_{\rm H}$ = 0.1

Notes. Collisions with H I are treated following to BBD10 = Barklem et al. (2010), BBS12 = Barklem et al. (2012), B13 = Belyaev (2013), BYB14 = Belyaev et al. (2014), BYG16 = Belyaev et al. (2016), Steenbock & Holweger (1984), with a scaling factor of $S_{\rm H}$.

Rybicki & Hummer (1991, 1992). An update of the opacity package in DETAIL was presented by Mashonkina et al. (2011).

3.2. Line selection, atomic data, and abundance determinations

The spectral lines used in the abundance analysis are listed in Table 3 together with their atomic parameters. The gf values are taken from VALD3, with the exception of Fe II, for which we used gf values from Raassen & Uylings (1998), which were corrected by +0.11 dex following the recommendation of Grevesse & Sauval (1999). The van der Waals broadening was accounted for by applying accurate data based on the perturbation theory (see Barklem et al. 2000, and references therein). Exceptions to this included Ca I, for which we employed the van der Waals damping constants, Γ_6, based on laboratory measurements of Smith (1981), and a few selected lines of Na I, Al I, Mg I, and Ba II, for which Γ_6 was estimated empirically from solar line-profile fitting by Gehren et al. (2004, Na I and Al I), Mashonkina (2013, Mg I), and Mashonkina et al. (2008, Ba II).

In VMP stars, aluminum can only be observed in the resonance doublet lines Al I 3944 and 3961 Å located in the spectral range, which is crowded even at such a low metallicity and rather noisy, in particular, in case of the dSph stars. The Al I 3944.006 Å line is heavily blended by the molecular CH 3943.85 and 3944.16 Å lines, and it was only used for an EMP star Scl031_11, which has low carbon abundance (Jablonka et al. 2015) and the best-quality observed spectrum. The second line, Al I 3961 Å, lies in the wing of Ca II 3968 Å and must be synthesised with a predetermined calcium abundance.

For the Si abundance determination, we preferred to employ Si I 4102 Å, which lies in the far wing of H_δ, but is not affected by any other atomic or molecular lines. However, for 9 stars in the dSphs and 12 MW stars with the best-quality spectra we also used Si I 3905.52 Å. This line is blended by the molecular CH 3905.68 Å line, and the Si abundance was derived either via spectral synthesis (six dSph stars) or by estimating a contribution of the CH line to the 3905 Å blend via spectral synthesis. The C/Fe abundance ratios were taken from Cohen & Huang (2010), Norris et al. (2010), Tafelmeyer et al. (2010), Cohen et al. (2013), and Jablonka et al. (2015). Our analysis of the CH 4310 Å band in the available spectra confirmed the literature data on [C/Fe]. It is worth noting that

Table 3. LTE and NLTE abundances from individual lines in the sample stars.

Atom	λ (Å)	E_{exc} (eV)	$\log gf$	$\log \Gamma_6/N_H$ (rad/s cm^3)	EW (mÅ)	$\log \varepsilon$ LTE	$\log \varepsilon$ NLTE
			ET0381				
Na I	5889.95	0.00	0.12	−7.670	173.0	3.51	3.19
Na I	5895.92	0.00	−0.19	−7.670	143.0	3.35	3.07
Mg I	5172.68	2.71	−0.45	−7.267	197.2	5.04	5.06
Mg I	5183.60	2.72	−0.24	−7.267	204.8	4.90	4.93
Mg I	5528.41	4.35	−0.50	−7.180	59.5	4.99	5.00
Al I	3961.52	0.01	−0.34	−7.315	−1	2.72	2.82

Notes. This table is available in its entirety in a machine-readable form at the CDS. A portion is shown here for guidance regarding its form and content. Γ_6 corresponds to 10 000 K. The sources of the observed equivalent widths, EWs, are indicated in Table 4. $EW = -1$ means using spectral synthesis.

the investigated dSph stars have low carbon abundance, with [C/Fe] ≤ 0. The exception is Boo-1137, with [C/Fe] = 0.25 (Norris et al. 2010). We evaluated the difference in the Si abundance derived without and with the CH line taken into account. This difference amounts to 0.32 dex for Boo-1137. The stars of the MW comparison sample were preselected by requiring [C/Fe] ≤ 0.

The best observed neutron-capture elements are strontium and barium. Unfortunately, even their abundances are not always accessible in our MW and dSph sample stars. This is partly because the observations did not cover the strongest lines of these elements located in the blue spectral range and partly because some spectra are too noisy in these regions. For example, Sr II 4077, 4215 Å are missing in the Boötes I spectra of Gilmore et al. (2013) and so are the Sr II and Ba II resonance lines in Scl07-49, HD 218857, and CD−24°1782. For several stars, the resonance lines of Sr II and/or Ba II could not be extracted from noise. This is the case of five stars in the Sculptor dSph, that is, 11_1_4296 and S1020549 from Simon et al. (2015) and 002_06, 031_11, and 074_02 from Jablonka et al. (2015), and a MW halo star HE1357-0123 from Cohen et al. (2013). We caution that we could not use the Ba II equivalent widths of Ural et al. (2015) as a consequence of strong inconsistencies between lines. For example, in UMi718, Ural et al. (2015) measured W_{obs} = 63.5 mÅ for Ba II 5853 Å (E_{exc} = 0.6 eV, $\log gf = -1$), while W_{obs} = 28.8 mÅ for Ba II 6496 Å (E_{exc} = 0.6 eV, $\log gf = -0.38$). For Ba II 4554 Å (E_{exc} =0, $\log gf = 0.17$) in UMi446, they give W_{obs} = 72.1 mÅ, but larger value of W_{obs} = 144.4 mÅ for Ba II 6496 Å.

For Sr II, we attempted to use both resonance lines when they were available. The Sr II 4215.539 Å line is notably blended by Fe I 4215.426 Å in the [Fe/H] > −3 stars and therefore was ignored in the abundance analysis, if Sr II 4077 Å was available. The case of Boo-127 ([Fe/H] = −1.93) is an exception to this rule. As in Frebel et al. (2016), the synthetic spectrum analysis results in a substantially lower abundance from Sr II 4077 Å, by 0.5 dex, compared with that from Sr II 4215 Å. The Sr abundance of Boo-127 was derived from Sr II 4215 Å.

The Ba II 4934 Å and 6141 Å lines are blended with some Fe I lines (see details in Jablonka et al. 2015). Whenever the spectrum was available, the Ba abundance was determined from spectral synthesis. Otherwise, the contribution of the Fe I lines to the blends at 4934 Å and 6141 Å was estimated by computing their synthetic spectra. When the blending between the Fe and Ba lines was substantial, then Ba II 6141 Å was not used.

The lines of Sr II, Ba II, and Eu II are composed of multiple components because each of these chemical elements is represented by several isotopes. For Sr II 4077 and 4215 Å, their isotopic splitting (IS) and hyper-fine splitting (HFS) structure is taken into account using the atomic data from Borghs et al. (1983) and the solar system Sr isotope abundance ratios from Lodders et al. (2009). The difference between the solar system and the r-process Sr isotope mixture (Arlandini et al. 1999) produces negligible effect on the derived stellar Sr abundances.

In contrast, the Ba abundance derived from the 4554 Å and 4934 Å resonance lines depends on the isotope mixture adopted in the calculations because of substantial separations of 57 and 78 mÅ, respectively, between the HFS components (Brix & Kopfermann 1952; Silverans et al. 1980; Blatt & Werth 1982; Becker & Werth 1983). Since the odd-A isotopes ^{135}Ba and ^{137}Ba have very similar HFS, the abundance is essentially dependent on the total fractional abundance of these odd isotopes, f_{odd}. The larger f_{odd}, the broader the resonance line is, and the greater energy it absorbs. In the solar system matter, f_{odd} = 0.18 (Lodders et al. 2009), however, larger value of f_{odd} = 0.438 (Kratz et al. 2007) to 0.72 (McWilliam 1998) is predicted for pure r-process production of barium. We inspected the influence of the f_{odd} variation on the Ba abundance determinations. In the four MW stars, with W_{obs}(4554 Å) ≤ 33 mÅ, the abundance derived from the Ba II resonance line is, in fact, insensitive to the adopted f_{odd} value. In Boo-1137, where W_{obs}(4934 Å) = 40.5 mÅ, and Leo IV-S1, where W_{obs}(4554 Å) = 62 mÅ, the abundance difference between using f_{odd} = 0.18 and 0.46 amounts to $\Delta \log \varepsilon$ = 0.03 dex and 0.05 dex, respectively. A notable shift of $\Delta \log \varepsilon$ = 0.18 dex was only found for HE0011-0035, with W_{obs}(4554 Å) = 104 mÅ.

Fortunately, the Ba II 5853, 6141, and 6497 Å subordinate lines are almost free of HFS effects. Therefore, in case the subordinate lines are available, they were used to derive the Ba abundance; the exception to this is Boo-1137, for which Ba II 6141 and 6497 Å are rather weak. No subordinate line could be measured for Leo IV-S1, HE0011-0035, HE0122-1616, HE1356-0622, HE1416-1032, HE2249-1704, and BS16550-087, and the Ba abundance was determined from the resonance lines, adopting f_{odd} = 0.46, as predicted by Travaglio et al. (1999) for the r-process Ba isotope mixture.

We were able to determine the Eu abundances for six dSph stars and 12 MW halo stars. For eight of these stars, we worked on the observed spectra and performed spectral synthesis of the Eu II lines. For the other stars, we used the equivalent widths published by Kirby & Cohen (2012, Scl 1019417),

Cohen & Huang (2010, UMi 28104, 33533, 36886, 41065, and JI19), and Cohen et al. (2013, four MW stars). For all, we properly accounted for the HFS and IS structure thanks to the data of Lawler et al. (2001).

3.3. Codes and model ingredients

In this study, the synthetic spectrum calculations were performed with the codes SIU (Reetz 1991) and SYNTHV_NLTE (Ryabchikova et al. 2016), which implement the pre-computed departure coefficients, $b_i = n_i^{\rm NLTE}/n_i^{\rm LTE}$, to calculate the NLTE line profiles for the NLTE species. Here, $n_i^{\rm NLTE}$ and $n_i^{\rm LTE}$ are the statistical equilibrium and thermal (Saha-Boltzmann) number densities, respectively, from DETAIL. The code SYNTHV_NLTE is integrated within the IDL BINMAG3[2] code, written by O. Kochukhov, finally allowing the user to determine the best fit to the observed line profile. A line list for spectral synthesis has been extracted from the Vienna Atomic Line Database[3] (VALD3; Ryabchikova et al. 2015). Our test calculations with the solar model atmosphere in a broad wavelength range (4209 Å to 9111 Å) proved that using two different codes, SIU and SYNTHV_NLTE + BINMAG3, does not produce systematic shifts in derived abundances, namely, the abundance difference never exceeds 0.03 dex.

For all other lines we use their equivalent widths. For each line, we first calculate the LTE abundance with the code WIDTH9[4] (Kurucz 2005, modified by Vadim Tsymbal, priv. comm.). The NLTE abundance is then obtained by applying the NLTE abundance correction, $\Delta_{\rm NLTE} = \log \varepsilon_{\rm NLTE} - \log \varepsilon_{\rm LTE}$, computed with the code LINEC (Sakhibullin 1983) that uses the LTE and NLTE level populations from DETAIL. Our test calculations with LINEC and WIDTH9 have proved that, for any given line, both codes lead to consistent LTE abundances within 0.01−0.02 dex.

In a similar homogeneous way, all the codes we used do treat continuum scattering correctly; i.e. we took scattering into account not only in the absorption coefficient, but also in the source function.

As in Paper I, we used the MARCS model structures (Gustafsson et al. 2008).

4. Stellar element abundances

The LTE and NLTE abundances of Na, Mg, Al, Si, Ca, Ti, Ni (only LTE), Sr, and Ba were determined for each star, provided that the corresponding lines could be measured. The obtained results are available in Table 3. Other chemical species measured in Jablonka et al. (2015), namely, Sc II, Cr I, Mn I, Co I, and Y II, are absent from our list because no NLTE calculations were performed in the literature for the atmospheric parameters of our interest.

4.1. Impact of NLTE on derived chemical abundances

Our NLTE calculations for Na I, Mg I, Al I, Si I, Ca I-II, Ti I-II, Fe I-II, Sr II, and Ba II show that the departures from LTE are different for each species, and, in general, depend on the stellar atmosphere parameters and element abundances. We stress that our procedure consistently accounts for both statistical equilibrium and radiative transfer: the SE (NLTE) calculations were iterated by varying the element abundance until agreement was reached between the resulting model spectra and the observed spectra. Figure 1 shows the differences between the average NLTE and LTE abundance – (NLTE−LTE) – for the individual stars. This difference is set to the NLTE abundance correction, $\Delta_{\rm NLTE}$, if we have one line, for example, for Al I and Si I.

We discuss various NLTE species by separating them depending on the dominant NLTE mechanism, but not in the order of their nuclear charge. The NLTE effects for Ti I and Fe I were described in our Paper I. We also show the NLTE−LTE abundance differences for Ti I and Fe I in this paper (Fig. 1). For the range of stellar atmosphere parameters investigated in this study, all the NLTE neutral species are minority species. For example, even Si I, which has the largest ionisation energy, $E_{\rm ion}$ = 8.15 eV, contributes about 10% to the total Si abundance in the line-formation layers of the model with $T_{\rm eff}$/log g/[Fe/H] = 4590/1.20/−2.9. The number density of these minority species easily deviates from thermodynamic equilibrium, when the intensity of the ionising radiation deviates from the Planck function.

As discussed in the NLTE papers referenced in Table 2, the main NLTE mechanism for Mg I, Al I, and Ca I is the ultraviolet (UV) over-ionisation. This results in the depletion of the atomic level populations and weakened spectral lines compared to the LTE case and thus in positive NLTE corrections.

4.1.1. Al I

The largest positive NLTE corrections are computed for the resonance lines of Al I. For example, $\Delta_{\rm NLTE}$(Al I 3961 Å) reaches 0.66 dex for Scl6_6_402 (4890/1.78/−3.66). The NLTE effects for Al I depend strongly on stellar $T_{\rm eff}$, log g, and metallicity (Al abundance), resulting in much larger dispersion of the abundance differences between NLTE and LTE at fixed [Fe/H] compared with that for the other species, as shown in Fig. 1. For example, the MW stars HE1356-0622 (4945/2.0/−3.45) and HE1416-1032 (5000/2.0/−3.23) have larger $\Delta_{\rm NLTE}$(Al I 3961 Å) by about 0.3 dex, compared with that for the stars of similar metallicity, but lower effective temperature, such as BS16550-087 (4750/1.5/−3.40) and HE0039-4154 (4780/1.6/−3.26).

4.1.2. Ca I

There is a clear metallicity trend of the NLTE effects for Ca I, with NLTE−LTE approaching 0.3 dex, when [Fe/H] is close to −4. A thorough discussion of the NLTE abundance corrections for an extended list of the Ca I lines can be found in Mashonkina et al. (2016).

We encountered a problem with the Ca I 4226 Å resonance line that gives a lower abundance than the subordinate lines. For example, for Scl031_11 (4670/1.13/−3.69), the abundance difference between Ca I 4226 Å and three subordinate lines amounts to $\Delta \log \varepsilon = -0.65$ in the LTE calculations and becomes even more negative (−0.87 dex) in NLTE. Mashonkina et al. (2007) have first reported a similar case for the [Fe/H] $\simeq -2$ dwarf stars, although with a smaller abundance difference. This problem was highlighted by Spite et al. (2012) for their sample of VMP giants and dwarfs. Our calculations show that, in the VMP atmospheres, the total NLTE effect is smaller for the resonance line than for the subordinate lines. Overall over-ionisation

[2] http://www.astro.uu.se/~oleg/download.html
[3] http://vald.astro.univie.ac.at/~vald3/php/vald.php
[4] http://kurucz.harvard.edu/programs/WIDTH/

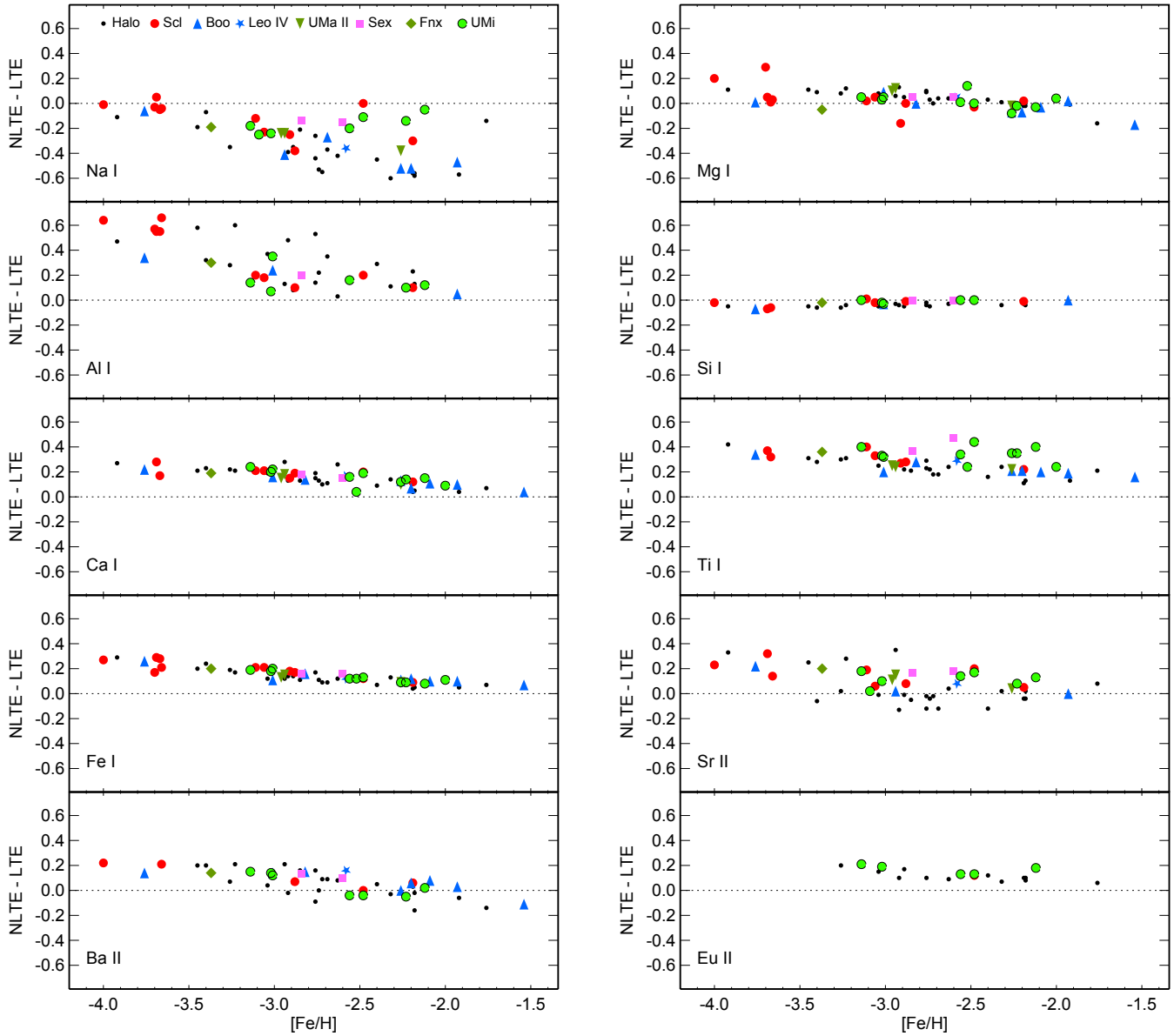

Fig. 1. Differences between the NLTE and LTE abundance of different chemical species in the Sculptor (red circles), Ursa Minor (green circles), Sextans (squares), Fornax (rhombi), Boötes I (triangles), UMa II (inverted triangles), and Leo IV (5 pointed star) dSph and the MW halo stars (small black circles).

of Ca I in deep atmospheric layers leads to weakened subordinate lines and line wings of Ca I 4226 Å. However, the core of Ca I 4226 Å forms in the uppermost atmospheric layers, where the departure coefficient of the upper level drops rapidly owing to photon escape from the line itself, resulting in dropping the line source function below the Planck function and enhanced absorption in the line core. This compensates in part or fully the NLTE effects in the line wings. For example, in the 4670/1.13/−3.69 model, Ca I 4226 Å has equal equivalent widths in NLTE and LTE.

As a consequence of the above considerations, we did not use Ca I 4226 Å for the abundance determinations. For Scl07-50 ([Fe/H] = −4.0), Scl6_6_402 ([Fe/H] = −3.66), and Scl11_1_4296 ([Fe/H] = −3.7), their Ca abundance is derived from Ca II 3933 Å. In these stars, $\Delta \log \varepsilon$(Ca II 3933 Å−Ca I 4226 Å) amounts to 0.59 dex, 0.15 dex, and 0.27 dex, respectively.

4.1.3. Mg I

As can be seen in Fig. 1, NLTE−LTE is mostly positive for Mg I. However, it is negative for Scl07-49 and Fnx05-42, where only the Mg Ib lines could be employed, and for the [Fe/H] > −2.4 stars, for which the used Mg I 4703 Å and 5528 Å lines are strong ($W_{\rm obs}$ > 100 mÅ). Strengthening the Mg Ib lines as compared to the LTE case was discussed in detail by Mashonkina (2013) in her analysis of HD 122563. The case is the same as that of Ca I 4226 Å reported in the previous subsection. We find that similar NLTE mechanisms act for Mg I 4703 Å and 5528 Å, when they are strong. Owing to competing NLTE mechanisms, NLTE−LTE for Mg I is overall small, less than 0.12 dex in absolute value; in the case of Scl07-50 and Scl11_1_4296, however, all the Mg I lines are weak and form in deep atmospheric layers that are subject to an over-ionisation of Mg I.

For Mg I, NLTE leads to smaller line-to-line scatter compared to the LTE case and cancels much of the scatter in [Mg/Fe]

between stars of close metallicities. Hereafter, the sample standard deviation, $\sigma_{\log\varepsilon} = \sqrt{\Sigma(\overline{x} - x_i)^2/(N_l - 1)}$, determines the dispersion in the single line measurements around the mean. For example, $\sigma_{\log\varepsilon} = 0.06$ dex in LTE and 0.03 dex in NLTE for HD 218857 (three lines of Mg I) and the abundance difference between HD 8724 ([Fe/H] = −1.76) and HD 218857 ([Fe/H] = −1.92) amounts to Δ[Mg/Fe] = 0.24 dex in LTE and 0.09 dex in NLTE.

4.1.4. Si I

Only small and mostly negative NLTE corrections are found for the Si I 3905 and 4102 Å lines, not exceeding 0.08 dex in absolute value. Indeed, with the accurate rate coefficients from Belyaev et al. (2014), the inelastic collisions with the neutral hydrogen atoms serve as an efficient thermalising process and largely cancel the over-ionisation effect for Si I in line formation layers.

4.1.5. Na I

In contrast to the photoionisation-dominated minority species, Na I is subject to over-recombination because the photon suction process prevails over the photoionisation that is inefficient for Na I due to small cross-sections of the ground state. The over-recombination results in strengthening the Na I 5889, 5895 Å lines and negative $\Delta_{\rm NLTE}$. The NLTE abundance corrections vary between −0.6 and −0.01 dex. An exception is Scl031_11 (4670/1.13/−3.69), for which the collision processes are inefficient compared to the photoionisation. Hence, the Na I lines are weaker than in LTE and NLTE−LTE = +0.05 dex.

In HD 8724 ([Fe/H] = −1.76) alone, we were able to measure not only the Na I resonance lines, but also the subordinate lines at 5682 and 5688 Å. The NLTE treatment of Na I substantially decreases the line-to-line scatter ($\sigma_{\log\varepsilon} = 0.05$ dex) compared with LTE, where $\sigma_{\log\varepsilon} = 0.10$ dex. A small abundance difference of −0.14 dex between NLTE and LTE for HD 8724 is explained by including in the abundance mean the subordinate lines, for which $\Delta_{\rm NLTE}$ is smaller in absolute value than that for the D_1, D_2 Na I lines, by 0.1 dex, and also by cooler $T_{\rm eff}$ of HD 8724 compared with that of the [Fe/H] ≃ −2 stars.

Similar to Al I, Na I shows a much larger scatter of (NLTE–LTE) at fixed [Fe/H] than the other species. This reflects a strong sensitivity of the departures from LTE for Na I to stellar log g, $T_{\rm eff}$, and the Na abundance. For example, at [Fe/H] > −2.7 some of the Ursa Minor (28104: 4275/0.65/−2.12), Sextans (11-04: 4380/0.57/−2.60), and Sculptor (1019417: 4280/0.5/−2.48) stars do not follow the metallicity trend in Fig. 1 that is defined by the Milky Way and Boötes I population because of the lower density of their atmospheres that weakens collisional coupling of the Na I high-excitation levels to the large continuum reservoir. For comparison, at [Fe/H] ≃ −2.2, HD 108317 and Boo-130 have log g = 2.96 and 1.4, respectively.

4.1.6. Sr II, Ba II, and Eu II

For the majority species such as Sr II and Ba II, NLTE may either strengthen or weaken the line depending on the stellar parameter and elemental abundance, as theoretically predicted by Mashonkina et al. (1999, Ba II) and Mashonkina & Gehren (2001, Sr II). In those MW halo giants, in which the Sr abundance follows the Fe abundance, the Sr II 4077 and 4215 Å resonance lines are strong and the departures from LTE are small, such that $\Delta_{\rm NLTE}$ varies between −0.15 and 0.08 dex. In the rest of the sample, the weaker the Sr II lines, the more positive NLTE correction is, up to $\Delta_{\rm NLTE} = 0.35$ dex.

A clear metallicity trend is seen in Fig. 1 for barium with negative NLTE−LTE for the [Fe/H] > −2 stars and positive NLTE−LTE for the majority of the VMP stars. Since a change in the sign of the NLTE abundance correction for Ba II lines depends on the stellar parameters and the element abundance itself, some of the [Fe/H] < −2 stars have slightly negative differences NLTE−LTE.

As discussed by Mashonkina & Gehren (2000), NLTE leads to weakened lines of Eu II and positive NLTE abundance corrections. In our cool giant sample, $\Delta_{\rm NLTE}$ grows slowly towards lower metallicity, but never exceeds 0.2 dex.

4.2. Nickel

Nickel is observed in lines of neutral atoms that are expected to be subject to over-ionisation like other minority species, such as Al I and Fe I. However, we cannot yet perform the NLTE calculations for Ni I because of the lack of a satisfactory model atom. Therefore, we assume that the ratio of abundances derived from lines of Ni I and Fe I is nearly free of the NLTE effects and use the LTE abundances in the [Ni I/Fe I] versus [Fe/H] diagrams. This assumption is supported by the fact that the ionisation energies of Ni I and Fe I are very similar, at 7.64 eV and 7.90 eV, respectively, and these atoms have similarly complicated term structures.

4.3. Outliers

In this section, we provide comments on a few stars that reveal peculiar abundances or any other outstanding feature.

Sculptor ET0381. This is an Fe-enhanced star, all measured chemical species being deficient relative to Fe. The LTE abundances were discussed in detail in Jablonka et al. (2015). We only find here small departures from LTE for most species. Despite an upward revision of [Fe/H], by 0.25 dex, leading to slightly changed [X/Fe] ratios, we confirm the conclusions of Jablonka et al. (2015). Except for [Ni/Fe], this star was not used in the calculations of the average [X/Fe] ratios of the Sculptor dSph.

Scl11_1_4296. In this star, the α-process elements Mg, Ca, and Ti reveal a different behaviour with respect to Fe, namely, [Mg/Fe] is as low as that of ET0381; however, [Ca/Fe] is higher compared with that of ET0381 and close to solar value. Titanium is enhanced relative to Fe, similar to the remaining Sculptor dSph stars. This star was not used in the calculations of the average [Mg/Fe] and [Ca/Fe] ratios of the Sculptor dSph.

Sex24-72. This is a carbon enhanced star. Tafelmeyer et al. (2010) determined [C/Fe] = 0.4, which applying the carbon correction from Placco et al. (2014) leads to an initial [C/Fe] ≃ 1. It reveals also high Na abundance with [Na/Fe] = 0.85 (NLTE). Combined with low abundance of the neutron-capture elements ([Sr/Fe] = −0.43, [Ba/Fe] = −1.04), Sex24-72 can be classified as a CEMP-no star.

Boo-041. We obtained higher iron abundance than that of Gilmore et al. (2013), by 0.42 dex, despite using common $T_{\rm eff}$ = 4750 K and log g = 1.6. This cannot be explained by NLTE effects because NLTE−LTE = 0.06 dex for Fe I. A difference of 0.25 dex in the average abundance from the Fe I lines appears already in LTE, as a consequence of lower microturbulence velocity, by 0.8 km s^{-1}, in our study. In the LTE calculations with $T_{\rm eff}$ = 4750 K, log g = 1.6, and $\xi_{\rm t}$ = 2.8 km s^{-1} determined by

Table 4. Summary of the LTE and NLTE abundances of the investigated stars.

Z	Atom	N_l	LTE				NLTE			Method of
			$\log\varepsilon$	$\sigma_{\log\varepsilon}$	[X/H]	[X/Fe]	$\log\varepsilon$	$\sigma_{\log\varepsilon}$	[X/Fe]	analysis
Sculptor ET0381, $T_{\rm eff}$ = 4570 K, log g = 1.17, [Fe/H] = −2.19, $\xi_{\rm t}$ = 1.7 km s^{-1}										
11	Na I	2	3.43	0.11	−2.90	−0.71	3.13	0.08	−1.01	$W_{\rm obs}$(JNM15)
12	Mg I	3	4.98	0.07	−2.60	−0.41	5.00	0.07	−0.39	$W_{\rm obs}$(JNM15)
13	Al I	1	2.72		−3.75	−1.56	2.82		−1.46	syn
14	Si I	2	4.80	0.04	−2.75	−0.56	4.79	0.01	−0.57	syn
20	Ca I	9	3.73	0.05	−2.63	−0.44	3.85	0.05	−0.32	$W_{\rm obs}$(JNM15)
22	Ti I	10	2.09	0.17	−2.84	−0.65	2.31	0.15	−0.43	idem
22	Ti II	21	2.60	0.17	−2.33	−0.14	2.60	0.17	−0.14	idem
26	Fe I	73	5.14	0.17	−2.36	−0.17	5.23	0.17	−0.08	idem
26	Fe II	9	5.31	0.09	−2.19	0.00	5.31	0.09	0.00	idem
28	Ni I	1	3.75		−2.50	−0.31				idem
38	Sr II	1	−0.18		−3.08	−0.89	−0.13		−0.84	syn
56	Ba II	2	−1.52	0.02	−3.65	−1.46	−1.46	0.02	−1.40	syn
Sculptor 002_06, $T_{\rm eff}$ = 4390 K, log g = 0.68, [Fe/H] = −3.11, $\xi_{\rm t}$ = 2.3 km s^{-1}										
11	Na I	2	2.72	0.16	−3.61	−0.50	2.60	0.11	−0.62	$W_{\rm obs}$(JNM15)
12	Mg I	5	4.57	0.06	−3.01	0.10	4.59	0.06	0.12	$W_{\rm obs}$(JNM15)

Notes. This table is available in its entirety in a machine-readable form at the CDS. A portion is shown here for guidance regarding its form and content.

References. JNM15 = Jablonka et al. (2015), syn = synthetic spectrum method.

Gilmore et al. (2013) and using 35 lines of Fe I with $E_{\rm exc}$ > 1.2 eV and $W_{\rm obs}$ < 180 mÅ, we obtained a steep negative slope of −0.41 for the $\log\varepsilon_{\rm FeI} - \log\ W_{\rm obs}/\lambda$ plot. Besides, the abundance difference $\log\varepsilon_{\rm FeI} - \log\varepsilon_{\rm FeII} = -0.22$ was uncomfortably large. We established $\xi_{\rm t}$ = 2.0 km s^{-1} by minimising the slope of the Fe I-based NLTE abundance trend with $W_{\rm obs}$. This also leads to consistent NLTE abundances from the two ionisation stages of iron within 0.11 dex. This star reveals an extremely high abundance of Ti, with [Ti/Fe] = 0.80, but a low abundance of Ni, with [Ni I/Fe I] = −0.52 (LTE). Boo-041 was not used in the calculations of the average [X/Fe] ratios. At [Fe/H] = −1.54, the Fe abundance of Boo-041 might have received the products of the type Ia supernova (SN Ia) nucleosynthesis.

4.4. Influence of uncertainties in stellar atmosphere parameters

Changes in the element abundances caused by a variation in $T_{\rm eff}$, log g, and $\xi_{\rm t}$ were evaluated for a part of our stellar sample in the earlier LTE analyses of Tafelmeyer et al. (2010, Table 4) and Jablonka et al. (2015, Tables 5 and 6) and the NLTE analyses of Mashonkina et al. (2010, Table 6) and Mashonkina et al. (2017, Sect. 4.2.4). When varying $T_{\rm eff}$, a differential NLTE effect on the derived abundance is the largest for Al I 3961 Å, however, it does not exceed 0.03 and 0.05 dex for $\Delta T_{\rm eff}$ = +100 K around $T_{\rm eff}$ = 4500 and 5000 K, respectively. Since the sample stars have similar temperatures and surface gravities, they also have similar abundance errors due to uncertainties in atmospheric parameters. To summarise, a change of +100 K in $T_{\rm eff}$ produces higher abundances from lines of the minority species, such as Mg I and Al I, by 0.10−0.15 dex, and has a minor effect (≤0.02 dex) on the abundances from lines of the majority species, such as Ti II and Sr II. In contrast, a change of +0.1 dex in log g has a minor effect (≤0.01 dex) on the minority species and shifts abundances of the majority species by up to +0.05 dex. A change of +0.2 km s^{-1} in $\xi_{\rm t}$ produces lower abundances, by 0.1 dex for the $EW \simeq 120$ mÅ lines and by 0.05 dex for the $EW \simeq 75$ mÅ lines.

5. Abundance trends and galaxy comparisons

Table 4 presents the elemental LTE and NLTE abundances together with their statistical errors and the number of lines used. For consistency with our previous studies, the solar photosphere abundances are those of Anders & Grevesse (1989) at the exception of Ti and Fe, for which we consider $\log\varepsilon_{\rm Ti,met}$ = 4.93 (Lodders et al. 2009, meteoritic abundance) and $\log\varepsilon_{\rm Fe,\odot}$ = 7.50 (Grevesse & Sauval 1998). The metallicities, [Fe/H], and the abundance ratios relative to iron, [X/Fe], are based on the Fe II lines. Our results are shown in Figs. 2–9.

5.1. α-process elements

For all α-process elements, we refer to their neutral species, except for Ti for which the abundance is based on lines of Ti II. Indeed the Ti II lines are more numerous and stronger than the Ti I lines. They are also less affected by any departure from LTE. In most of our sample stars, however, the abundances derived from the lines of Ti I and Ti II are consistent, as shown in Paper I.

Before going further, it is probably worth commenting on the consequence of choosing Fe II or Fe I as a metallicity indicator on the [X/Fe] versus [Fe/H] diagrams. Indeed, the vast majority of the published LTE analyses are provided in function of [Fe I/H]. This is a consequence of the fact that the number of Fe I lines is classically much larger in the observed wavelength range. As shown in Fig. 1, the LTE treatment underestimates the iron abundance, if it is based on the Fe I lines, and NLTE−LTE (Fe I) rises towards lower metallicity. For Ca I, NLTE−LTE follows a similar trend and magnitude as Fe I, hence NLTE leaves their ratios nearly unchanged compared with LTE. Conversely, because the NLTE corrections for Mg I and Si I are minor over the [−4, −1] metallicity range, [Mg I/Fe I] and [Si I/Fe I] are shifted downward in NLTE as compared to LTE.

Now, choosing Fe II as a metallicity indicator, [Mg I/Fe II], [Si I/Fe II], and [Ti II/Fe II] change only a little from LTE to

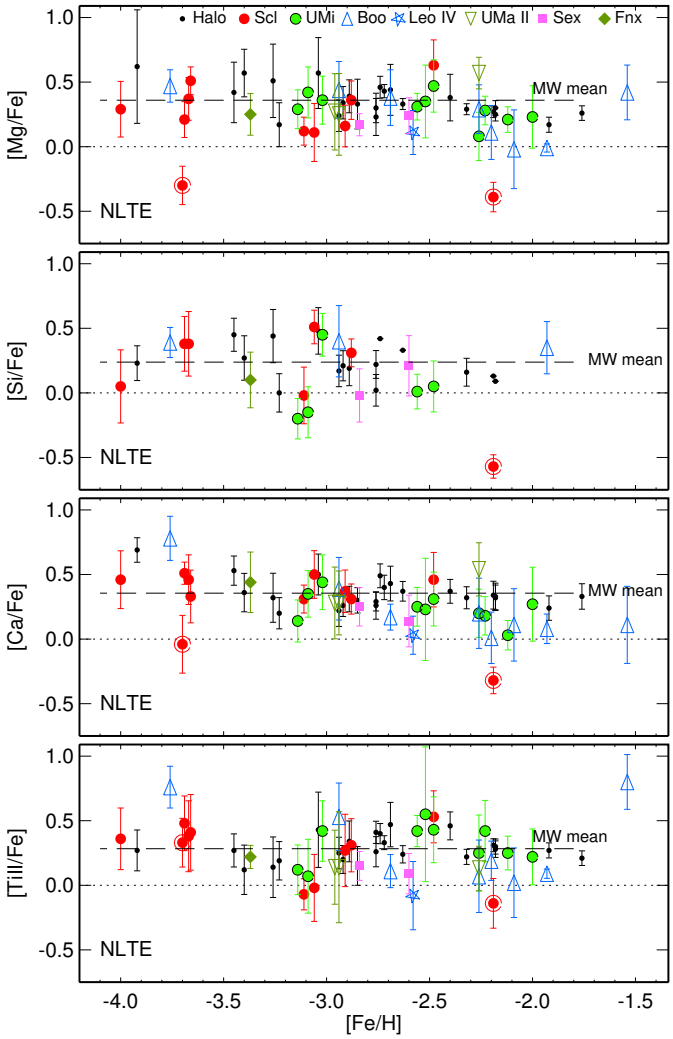

Fig. 2. Stellar element-to-iron NLTE abundance ratios for the α-process elements Mg, Si, Ca, and Ti in the Sculptor (red circles), Ursa Minor (green circles), Sextans (squares), Fornax (rhombi), Boötes I (triangles), UMa II (inverted triangles), and Leo IV (5 pointed star) dSphs and the MW halo. Two Mg-poor stars in Sculptor, 11_1_4296 and ET0381, are plotted by a red circle inside larger size open circle. The error bars were computed as $\sigma_{X/Y} = \sqrt{\sigma_X^2 + \sigma_Y^2}$. The errors of [Fe/H] do not exceed 0.15 dex for most (51 of 59) stars. In each panel, the dashed line indicates the mean for the MW halo.

NLTE, while [Ca I/Fe II] moves upward because of the positive NLTE corrections for Ca I.

Because we have obtained consistent Fe I- and Fe II-based abundances in the NLTE treatment (Paper I), our NLTE abundance ratios [X/Fe] do not depend on the choice of the metallicity tracer.

A remarkable gain of using the NLTE abundances based on a homogeneous set of atmospheric parameters is the reduction, compared to a simple compilation of the literature data (see Figs. 8 and 9 in Jablonka et al. 2015), of the spread in abundance ratios at given metallicity within each galaxy and from one to the other. This effect is particularly dramatic for Si for which the dispersion goes from a +1 dex down to ~0.2 dex once the Si and Fe abundances have been homogeneously revised.

Figure 2 shows that, at [Fe/H] ≤ -2.5, all galaxies scatter around the mean of the Milky Way halo stars, [α/Fe] $\simeq$ 0.3. Table 5 summarises the mean elemental ratios and their

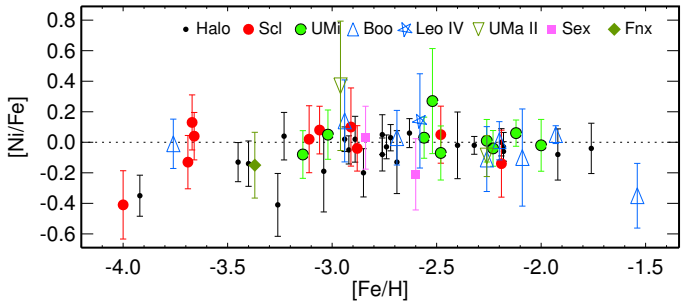

Fig. 3. Stellar [Ni I/Fe I] LTE abundance ratios. Symbols as in Fig. 2.

dispersions for the three galaxies with a sufficient number of stars: Sculptor, Ursa Minor, and the MW halo. The outliers of Sect. 4.3 are not considered in these calculations. These numbers quantify the small star-to-star scatter (~0.2 dex) and show that all α-elements have similar [X/Fe] means. The only apparent exception to this rule is the solar value of [Si/Fe] in Ursa Minor. For the JI19 star, which is the only star in this galaxy with two accessible Si I lines, [Si/Fe] = 0.45 ($\sigma_{\log\varepsilon}$ = 0.07 dex) is close to [X/Fe] for the other α-elements. The four other stars in Ursa Minor have only one Si I line at 4102 Å, which is located in a noisy region and leads to a solar or subsolar [Si/Fe] ratio. Our results for the MW giants are fully consistent with the NLTE abundances derived for the MW halo dwarfs by Zhao et al. (2016).

Previous LTE abundance analyses conducted at similar high spectral resolution and signal-to-noise ratios by Tafelmeyer et al. (2010), Starkenburg et al. (2013), Jablonka et al. (2015), and Simon et al. (2015) deduced a common conclusion that the Sculptor, Sextans, and Fornax dSphs are α-enhanced in the VMP regime at a similar level as the MW halo. On the other hand, lower [Ca/Fe] and [Ti/Fe] than [Mg/Fe] ratios were reported by Venn et al. (2004) and Cohen & Huang (2010) for the VMP stars in the Sextans and Ursa Minor dSphs. In part, these discrepancies can be caused by applying the LTE assumption. In case of using lines of Ti I and Fe I, LTE underestimates [Ti/Fe] because of larger departures from LTE for the Ti I than for the Fe I lines. In contrast, [Mg I/Fe I] is overestimated in the LTE analysis, as discussed in the beginning of this section. Our homogeneous NLTE analysis removes discrepancies in [X/Fe] between different α-elements and between the classical dSphs and MW halo.

We have three ultra-faint galaxies ($L \leq 10^5\ L_\odot$) in our sample: Ursa Major II, Leo IV, and Boötes I. Interestingly, they present different features. In Ursa Major II, the three stars with very different metallicities, between [Fe/H] $\simeq -3$ and -2.3, are α-enhanced. In contrast, Leo IV and Boötes I, which are the brightest of the Local Group UFDs (McConnachie 2012), reveal a close-to-solar α/Fe ratio at [Fe/H] $\gtrsim -2.5$. Gilmore et al. (2013) had reported on a hint of a decline in [α/Fe] but found this decline not yet "formally significant". The existence of a low [α/Fe] population is now put on a firm ground with consistent evidence from the three elements, Mg, Ca, and Ti, for which data are available. We commented earlier that Boo-041 cannot be accounted for the bulk of Boötes I population. The kinematics and morphology of Boötes I point towards a complex system (Koposov et al. 2011; Roderick et al. 2016). But as far as chemical evolution is concerned, Boötes I, and potentially Leo IV as well, seem to simply push back the frontier at which galaxies can reprocess the SNeIa ejecta; these galaxies have a knee at lower metallicity than their more massive counterparts, as expected from a classical chemical evolution. So far the galaxies, in which a knee in [α/Fe] has been found,

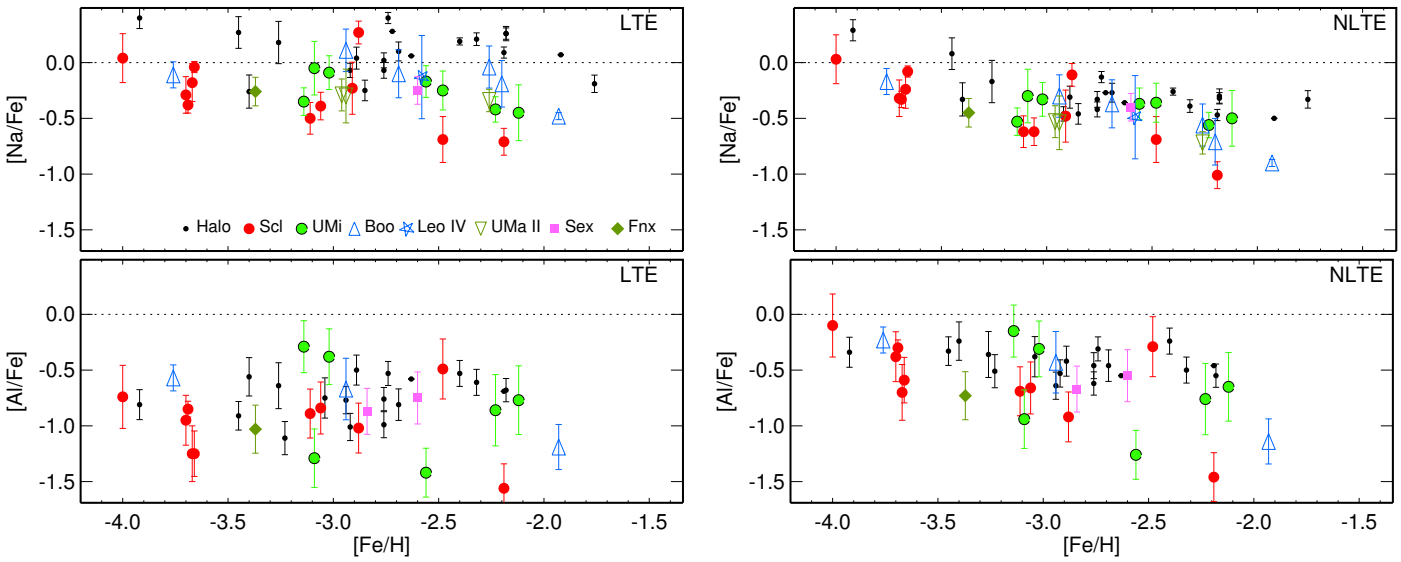

Fig. 4. Stellar [Na/Fe] and [Al/Fe] LTE (*left column*) and NLTE (*right column*) abundance ratios. The LTE and NLTE ratios of [Na/Fe] = 0.99 and 0.85, respectively, for Sex 24-72, are not shown. Symbols as in Fig. 2.

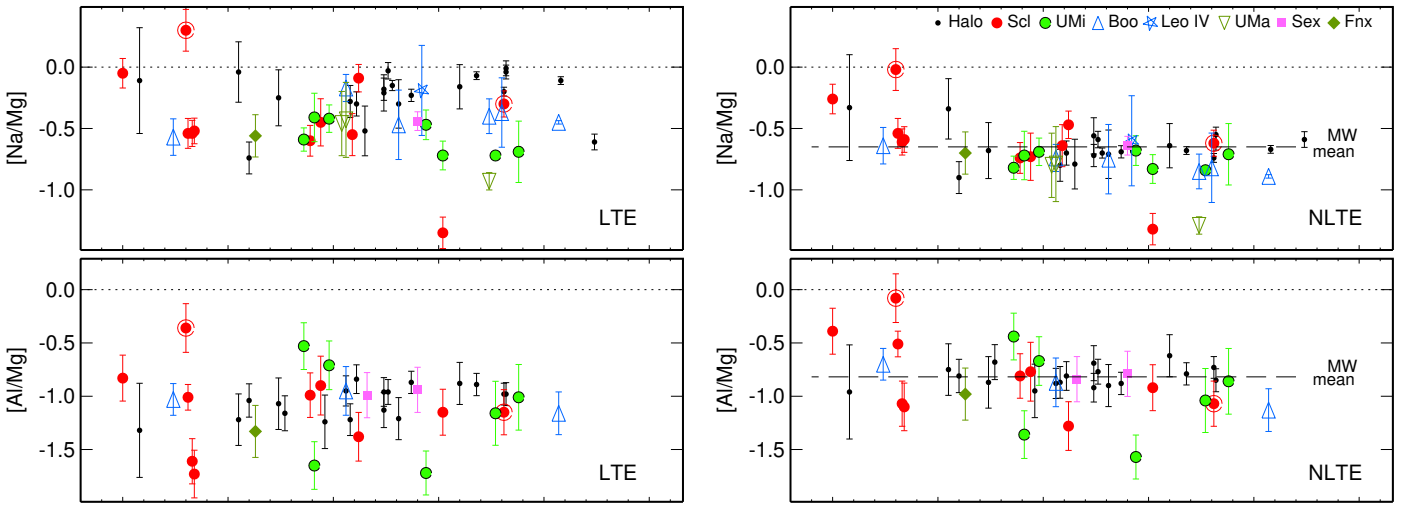

Fig. 5. Stellar [Na/Mg] and [Al/Mg] LTE (*left column*) and NLTE (*right column*) abundance ratios. The NLTE ratio [Na/Mg] = 0.68 for Sex 24-72 is not shown. Symbols as in Fig. 2.

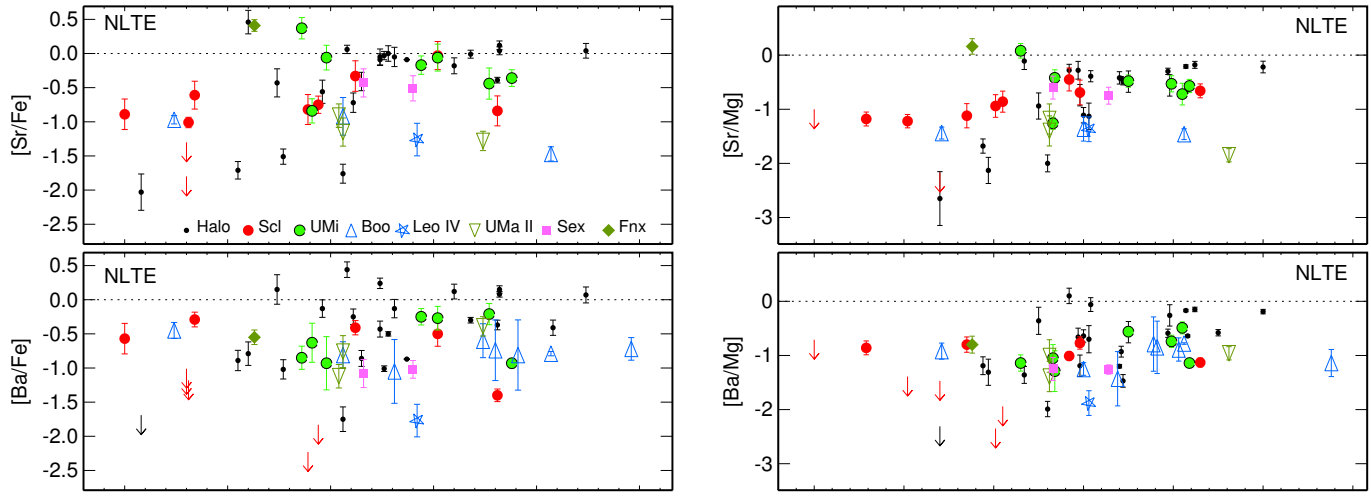

Fig. 6. *Left column*: [Sr/Fe] and [Ba/Fe] NLTE abundance ratios as a function of metallicity for our sample stars. *Right column*: [Sr/Mg] and [Ba/Mg] NLTE abundance ratios as a function of Mg abundance. Symbols and colours are as in Fig. 2. Upper limits in the Ba and Sr abundances are indicated with arrows.

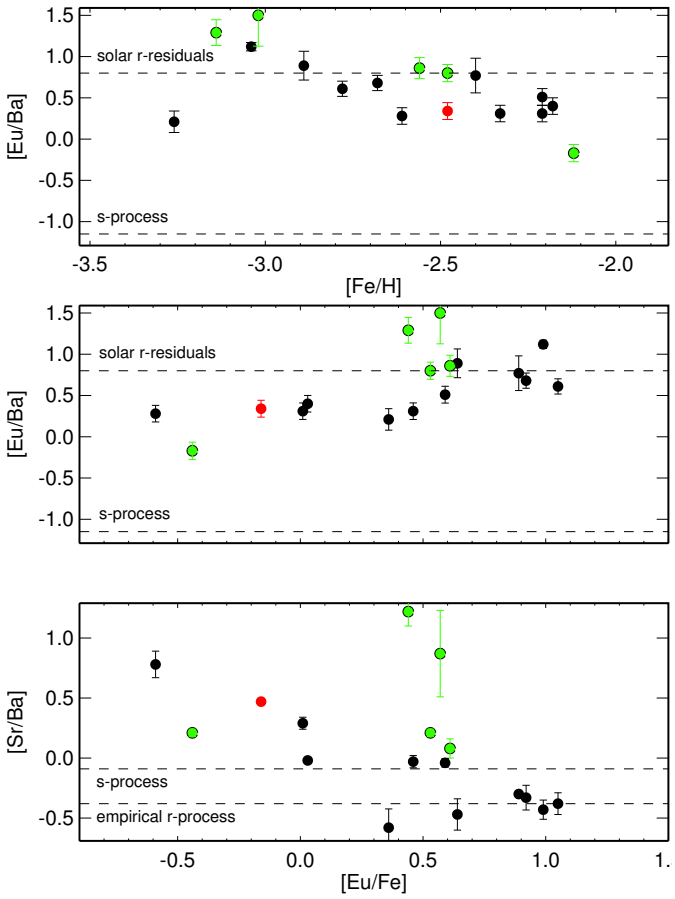

Fig. 7. Stellar [Eu/Ba] (*top and middle panels*) and [Sr/Ba] (*bottom panel*) NLTE abundance ratios in the MW halo (black circles) and the Sculptor (red circle) and Ursa Minor (green circles) dSphs. The dashed lines indicate the r- and s-process ratios $[Eu/Ba]_r = 0.80$, $[Eu/Ba]_s = -1.15$, and $[Sr/Ba]_s = -0.09$ according to Bisterzo et al. (2014) and our empirical estimate of $[Sr/Ba]_r = -0.38$.

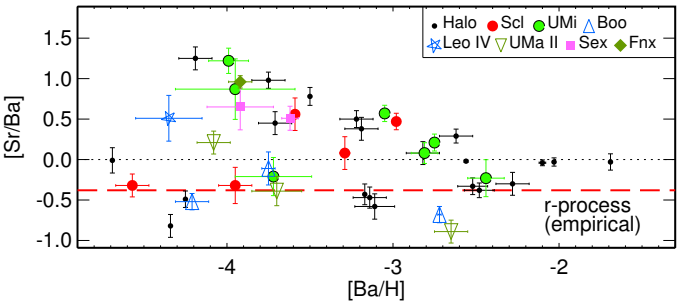

Fig. 8. [Sr/Ba] NLTE abundance ratios as a function of Ba abundance. The dashed line indicates the mean [Sr/Ba] ratio of the six r-II stars (see text). Symbols and colours are as in Fig. 6.

had star formation histories of a few Gyr long, while those of Boötes I and Leo IV are shorter (Okamoto et al. 2012). However, the nature and timescale of the type Ia supernovae are still under investigation (Kobayashi & Nomoto 2009; Nomoto et al. 2013), and there is evidence that metal-poor environments have their own specific features (Taubenberger et al. 2011). Given that star formation proceeds in series of very short timescale bursts (~0.1 Gyr, Revaz & Jablonka 2012), it is very possible that Boötes I had enough time to form stars after its first SN Ia explosions provided that the latter occur on short timescales. The chemical evolution models by Romano et al. (2015) have

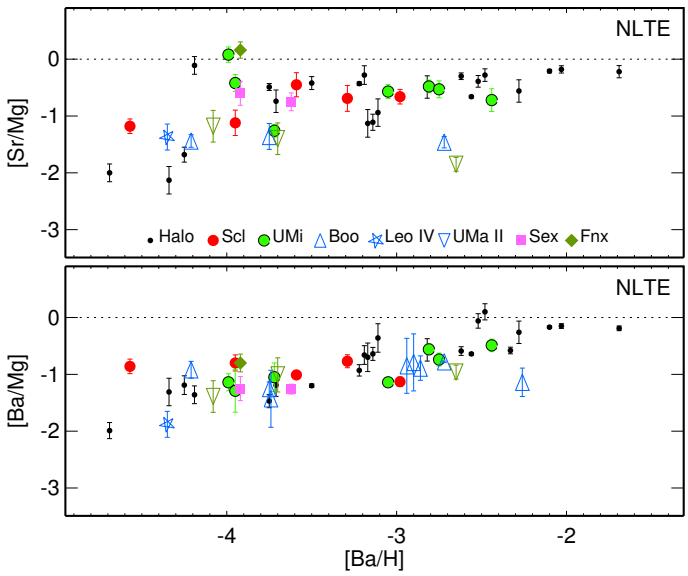

Fig. 9. [Sr/Mg] and [Ba/Mg] abundance ratios vs. [Ba/H]. Symbols as in Fig. 6.

Table 5. Average NLTE abundance ratios for different stellar populations, with $\sigma_{X/Fe}$ indicated in parentheses.

[X/Fe]	Sculptor	Ursa Minor	MW halo
[Mg/Fe]	0.31 (0.19)	0.30 (0.11)	0.36 (0.13)
[Si/Fe]	0.25 (0.21)	0.03 (0.26)	0.24 (0.15)
[Ca/Fe]	0.41 (0.08)	0.24 (0.11)	0.36 (0.11)
[Ti/Fe]	0.30 (0.19)	0.32 (0.16)	0.28 (0.10)

allowed some SNeIa to be exploded in Boötes I while it was still forming stars. An alternative possibility is that low mass SNeII have particularly contributed to the chemical evolution of the galaxy (Webster et al. 2015).

5.2. Nickel

As discussed in Sect. 4.2, we did not treat Ni in NLTE. Nevertheless, we think that the [Ni I/Fe I] versus [Fe/H] trend is relevant to this work. Figure 3 shows that the yields of Ni and Fe have a constant ratio and the correlation is reasonably tight. It is, in fact, tighter than with any other element produced by SNeII. Both dSph and MW halo stars are distributed around [Ni/Fe] = 0. Our sample appears to avoid the high [Ni/Fe] stars reported by Roederer (2009). Given the large range of galaxy masses that we are sampling, this is very remarkable. The only trend with metallicity is the increased dispersion at $[Fe/H] \leq -3$, that is, 0.15 dex instead of 0.08 dex above [Fe/H] = −3, which could well be explained by increasing the abundance uncertainties due to the weakening the Ni I lines.

5.3. Odd-Z elements: Na and Al

The impact of NLTE is particularly large on the elemental ratios involving Na and Al, as a consequence of large NLTE abundance corrections for lines of Na I and Al I and their extreme sensitivity to each of the stellar parameters. The star-to-star scatter in the [Na/Fe] (Fig. 4) and [Na/Mg] (Fig. 5) NLTE abundance ratios is much smaller than in the LTE abundance ratios. For [Al/Fe] and [Al/Mg], the scatter is larger for the dSph than the MW stars;

this is most probably due to the lower S/N ratio of the observed blue spectra and the uncertainty in the analysis of Al I 3961 Å.

The Milky Way and dSphs reveal indistinguishable trends in metallicity for [Na/Fe], [Na/Mg], and [Al/Mg], which suggests that the nucleosynthesis processes for Na and Al (carbon burning process) are identical in all systems, independent of their mass. This is in contrast to LTE, for which we obtain systematically higher [Na/Fe] and [Na/Mg] ratios for MW stars than for dSph stars by about 0.4 and 0.3 dex, respectively. It seems that the early production of sodium occurred in a similar way to that of the primary elements. This is confirmed by the constant [Na/Mg] $\simeq -0.6$ and [Al/Mg] $\simeq -0.8$ ratios in Fig. 5. The only exception to this rule is Scl11_1_4296, whose high [odd-Z/Mg] ratios are only due to its depletion in Mg. The ET0381 star does not stand out in [odd-Z/Mg], meaning that its Al, Na, and Mg were produced in similar relative amounts, as these elements in the other stars.

We confirm the existence of a plateau in [Na/Fe] at [Fe/H] ≤ -2.0 shown in Andrievsky et al. (2007). These authors reported a mean value of [Na/Fe] = −0.2, while we find [Na/Fe] = −0.4. The difference between the two studies probably arises from the fact that Andrievsky et al. (2007) used the iron LTE abundances and, hence, underestimated [Fe/H] values. Just as we did here, Andrievsky et al. (2007) showed a hint of a rise in [Na/Fe] below [Fe/H] = −3.5. As discussed in Paper I, the NLTE ionisation balance between Fe I and Fe II is not fully satisfied for the Sculptor stars in this region. Hence we might actually underestimate [Fe/H] by a bit by referring to Fe II. The Milky Way star at [Fe/H] = −3.92, HE1357-0123, with more than 0.2 dex difference between its Fe I- and Fe II-based abundances, also follows the [Na/Fe] rising trend, calling for further investigation.

Going from LTE to NLTE dramatically changes the picture of early enrichment of the MW and the dSphs in Na and Al. In NLTE, we found sodium to be slightly overabundant relative to aluminum with the mean of [Na/Al] ∼ 0.2 dex, while we obtained a substantially larger ratio of [Na/Al] ∼ 0.8 in LTE.

For clarity, we do not include a carbon-enhanced star Sex24-72 in the [Na/Fe] panel of Fig. 4. This is one of the very rare CEMP-no stars found in a classical dSph (Skúladóttir et al. 2015). Tafelmeyer et al. (2010) have measured $^{12}C/^{13}C = 6$ in this star, a clear indication of internal mixing (see, for example, Spite et al. 2006). We determine [Na/Fe] = 0.85, [Na/Mg] = 0.68, and [Na/Al] = 1.52, hence, a clear overabundance of sodium. Unlike the mixed stars in Spite et al. (2006), the [Al/Mg] ratio of Sex24-72 does not stand out from our other sample stars, and this star is not particularly Mg poor. Therefore, the abundance pattern of Sex24-72 was not affected by the Mg-Al cycle. We conclude that the Na overabundance of Sex24-72 is a consequence of the extra mixing between the atmosphere and the H-burning shell, which was deep enough to bring the products of the Ne-Na cycle to the surface.

5.4. Neutron-capture elements: Sr and Ba

Despite many theoretical and observational studies of the neutron-capture elements in the long-lived stars in our Galaxy, some questions remain unanswered. For example, we seek to understand what is (are) the astrophysical site(s) of the rapid (r) process of neutron-capture nuclear reactions; what types of nuclear reactions produced the light trans-iron elements, Sr-Zr, in the early Universe; and whether the light and heavy (beyond Ba) elements originate from a common astrophysical site and, if so, at which site(s).

It is beyond the scope of this work to provide any definitive answers. However, the homogeneity of our abundance analysis and our compilation of galaxies with very different evolutionary paths provide a few clear pieces of evidence that can constrain future models.

The left panels of Fig. 6 present the variation of Ba and Sr relative to Fe as a function of metallicity in a classical manner. At first glance both [Sr/Fe] and [Ba/Fe] present a very large scatter at any given [Fe/H]. A closer look, nevertheless, reveals different behaviours, which depend on the metallicity range and on the galaxy: i) [Fe/H] $\simeq -2.8$ is a metallicity threshold below and above which the dispersion in abundance ratio changes and ii) massive and fainter galaxies do not follow the same trend.

We first concentrate on our MW halo sample. In both LTE and NLTE abundance analyses, [Sr/Fe] and [Ba/Fe] have large dispersion below [Fe/H] $\simeq -2.8$, as also shown by Andrievsky et al. (2009, 2011) and Hansen et al. (2013). Above this metallicity, [Sr/Fe] becomes steadily solar. As to [Ba/Fe], the rise to the solar value comes at slightly higher metallicity, [Fe/H] $\simeq -2.5$. Although largely diminished, the dispersion is larger than for [Sr/Fe].

Europium abundances are available for 11 stars of our MW sample and, in particular, for all stars at [Fe/H] > -2.5. The exception is HD 218857 ([Fe/H] = −1.92) because its spectrum does not extend far enough into the blue wavelength. Figure 7 shows that all these stars have [Eu/Ba] ≥ 0.28, which is a value much closer to the r-process $[Eu/Ba]_r = 0.80$ (based on the solar r-residuals; Bisterzo et al. 2014) than the s-process $[Eu/Ba]_s = -1.15$ ratio. This reflects the fact that if the s-process contributes to the Ba abundances, it is only a minor contribution. We discard the most metal-rich star of our sample, HD 8724, with [Fe/H] = −1.76 and [Eu/Ba] = 0.21, from any discussion on very metal-poor stars.

If Ba and Sr were produced by the same nucleosynthesis source, this would result in a fairly flat (within observational error bars) [Sr/Ba] ratio versus [Ba/H]. This is clearly not the case in Fig. 8. Our MW halo sample is separated into two groups. The first group includes 8 of 20 stars and indeed has similar [Sr/Ba] ∼ −0.5 for the entire range of Ba abundances. Although the astrophysical site(s) of the r-process is (are) not identified yet (Wanajo et al. 2014; Nishimura et al. 2017), the strongly r-process enhanced ([Eu/Fe] > 1, [Eu/Ba] > 0) stars referred to as r-II stars (Christlieb et al. 2004) provide observational evidence for the r-process to yield a subsolar Sr/Ba ratio. We estimate the empirical r-process ratio, $[Sr/Ba]_r = -0.38$, using the six halo r-II stars: CS 22892-052 (Sneden et al. 2003), HE1219-0312 (Hayek et al. 2009), SDSS J2357-0052 (Aoki et al. 2010), HE2327-5642 (Mashonkina et al. 2010), CS 31082-001 (Siqueira Mello et al. 2013), and CS 29497-004 (Hill et al. 2017). It is worth noting that a sample of 253 metal-poor halo stars in Barklem et al. (2005) includes eight r-II stars; these eight stars all have the lowest and similar Sr/Ba, with the mean $[Sr/Ba]_{r-II} = -0.44 \pm 0.08$ that is very close to our estimate of $[Sr/Ba]_r$. The question is whether the observed subsolar Sr/Ba ratio itself can be considered as a signature of the r-process origin of Sr.

The second MW group seems to be aligned on a well-defined downward trend of [Sr/Ba] with [Ba/H]. Similar tight anti-correlation of [Sr/Ba] with [Ba/Fe] and [Ba/H] was reported by Honda et al. (2004) and François et al. (2007). In line with Barklem et al. (2005), we obtained that an enhancement of Sr relative to Ba correlates with the stellar Eu abundance (Fig. 7): no star with supersolar Sr/Ba ratio is enhanced in Eu, while the stars with subsolar Sr/Ba ratios have [Eu/Fe] ≥ 0.36.

In order to explain an excess of Sr production relative to the classical r-process, various ideas and models have been proposed: i) the weak s-process during the hydrostatic core He-burning phase of massive stars (Raiteri et al. 1991); ii) charged particle reactions in core-collapse supernovae (Woosley & Hoffman 1992); iii) nucleosynthesis from progenitor stars that lived and died prior to the formation of the first "main" r-process stars (Truran et al. 2002); iv) non-standard s-process in low-metallicity massive rotating stars (Pignatari et al. 2008); v) explosive nucleosynthesis in a high energy SN (or "hypernova") (Izutani et al. 2009); vi) rapid charged-particle reactions in the high-entropy winds at low entropies (Farouqi et al. 2010); vii) neutron star mergers (Tsujimoto & Shigeyama 2014; Wanajo et al. 2014); viii) the weak r-process (referred also to as alpha-process) taking place in neutrino-driven winds (Bliss et al. 2017); and ix) the intermediate r-process in core-collapse supernovae driven by the magneto-rotational instability (Nishimura et al. 2017). However, the source(s) is (are) not identified yet.

The confrontation of galaxies with very different star formation histories and chemical evolution paths provides new abundance trends and should help to constrain the nucleosynthesis origins of the neutron-capture elements.

We find differences in the abundance trends between classical dSphs (Sculptor, Ursa Minor, Fornax, and Sextans) and UFDs (Boötes I and UMa II) and differences between the elemental ratios involving Sr and Ba for classical dSphs. The main observational results can be summarised as follows.

Keeping the same distinctive two regions below and above [Fe/H] $\simeq -2.8$, -2.5 for Sr and Ba, respectively, Fig. 6 shows that the classical dSph and the MW halo stars behave identically in the low-metallicity regions, with large dispersions in [Sr/Fe] or [Ba/Fe] in both cases.

In the two UFDs, Boötes I and UMa II, all the stars are depleted in Sr and Ba relative to Fe, with very similar ratios of [Sr/Fe] $\simeq -1.1$ and [Ba/Fe] $\simeq -0.75$ on the entire range of metallicity (Fig. 6). Their Ba/Fe ratio is close to the Ba/Fe floor of the MW halo, while Sr/Fe is higher than that for the most Sr-poor stars in the MW, by more than 0.5 dex. The Sr/Fe ratio of the only star available in Leo IV-S1 does not stand out of the corresponding ratios in Boötes I and UMa II, but Ba/Fe is lower, by one order of magnitude, although remains at the level of Ba/Fe for the MW most Ba-poor stars. Low [Ba/Fe] ratios had been reported by Frebel et al. (2010) and Kirby & Cohen (2012) based on their LTE analyses. The improvement here is that homogeneity of the analysis allows us to accurately compare the levels of the stellar abundance ratios.

In order to put all galaxies on the same footing and, in particular, to remove any potential pollution of the iron abundances by the ejecta of SNeIa that would affect some galaxies at [Fe/H] ≥ -2.8 but not the others, we now consider the evolution of Ba and Sr relatively to Mg, as shown in the right panels of Fig. 6. The same conclusions, as drawn below, would be reached should one consider any other α-element.

The dichotomy seen previously remains. The large scatter of data below [Mg/H] $\simeq -2.6$ in the massive galaxies confirms that their early enrichment in Ba and Sr is produced in a variety of conditions, which are sufficiently rare and with varying yields for the interstellar medium to remain inhomogeneous. A more ordered behaviour of Sr/Mg and Ba/Mg is observed above [Mg/H] $\simeq -2.6$. Strontium and barium present different features though.

There are two clear sequences at [Mg/H] $\gtrsim -2.6$ for Sr/Mg. One sequence scatters around [Sr/Mg] $\simeq -0.37$, which gathers the MW halo stars and the most massive (classical) dwarfs, such as Sextans, Ursa Minor, and Sculptor. The UFDs Leo IV, UMa II, and Boötes I, however, maintain remarkably consistent and low abundance ratios at the level of [Sr/Mg] $\simeq -1.3$. This means that while the stellar population of massive dSphs and the MW halo can increase their abundance of Sr relatively to Mg, the UFDs cannot and thereby, miss this additional Sr production channel.

As to Ba, again similar ratios, at the level of [Ba/Mg] ~ -1, are found in the UFDs Boötes I and UMa II on the entire Mg abundance range. In the classical dSphs, the scatter of Ba/Mg is reduced above [Mg/H] $\simeq -2.4$, but much less than for Sr/Mg, and one does not witness any particular differential behaviour between the classical and faint dwarfs. While the dSph stars populate [Ba/Mg] regions where one finds the MW stars as well, it is fair to say that they do not reach as high ratios as our MW sample stars.

Previous LTE observational investigations that compare dwarf spheroidal galaxies with the Milky Way halo population have shown evidence for more than one channel of production of the neutron-capture elements lighter than Ba (Cohen & Huang 2010; Frebel et al. 2010; Tafelmeyer et al. 2010; Kirby & Cohen 2012; Jablonka et al. 2015; Roederer 2017). However, at this stage the question of the different production origins is still wide open. Our goal in the following is to provide concrete evidence and constraints that can be further used to improve theoretical models.

Since neither Fe nor Mg are good tracers for heavy or light neutron-capture elements, we examine the Sr/Ba ratio as a function of [Ba/H] (Fig. 8).

For the UFDs, the statistics of Sr/Ba is even poorer than that for the Sr abundances. Five of our seven stars in the UFDs with such measurements have subsolar [Sr/Ba], -0.11 down to -0.89, suggesting a common origin of the neutron-capture elements in the Boötes I and UMa II stars in the classical main r-process. The analysis of the r-process-rich galaxy Reticulum II has provided evidence for a variety of evolution among UFDs and a reference to the r-process enhanced stars in these systems, which have similar [Sr/Ba] ratios of -0.21 to -1.17 (Ji et al. 2016; Roederer et al. 2016).

The classical dSphs follow the trends defined by the MW halo stars, either at subsolar [Sr/Ba] or along the upward [Sr/Ba] trend with decreasing [Ba/H]. In the Sculptor dSph, the upward trend extends probably to [Ba/H] ~ -5. Indeed, we have the two stars, Scl002_06 and Scl074_02, where the Ba II 4934 Å resonance line could not be measured resulting in [Sr/Ba] > 1.1, while their [Ba/H] $\lesssim -5$. For our MW sample, the statistics of Sr/Ba measurements at [Ba/H] < -4 is poor, however, the upward [Sr/Ba] trend extending down to [Ba/H] $\simeq -5$ was reported by Honda et al. (2004).

The well-delineated branch at [Sr/Ba] ≥ 0 is built from stars of increasing Ba and stable Sr abundances. This is seen in Fig. 6 (right column) and even more clearly in Fig. 9. For these stars, the [Sr/Mg] ratios are nearly flat over the $-4 \lesssim$ [Ba/H] $\lesssim -2.5$ range, while [Ba/Mg] is substantially lower than [Sr/Mg] at [Ba/H] $\simeq -4$, but approaches [Sr/Mg] at the highest Ba abundances. We thus infer that the second producer of strontium in the MW halo and the classical dSphs was independent of the production of barium and operated below [Ba/H] ~ -4.

6. Conclusions

The aim of this paper is to provide the community with a robust framework for galaxy chemical evolution studies. For that purpose, we assembled a sample of galaxies with very different

evolutionary paths, benefiting from high-resolution spectroscopy ($R \geq 25\,000$) from a variety of sources. In Paper I we presented a homogeneous set of accurate atmospheric parameters. In this study, we determined the NLTE abundances of 10 chemical species in giant stars covering the $-4 <$ [Fe/H] < -1.7 metallicity range and belonging to the Milky Way halo (23 stars), to the Sculptor, Ursa Minor, Sextans, and Fornax classical dSphs, and to the Boötes I, UMa II, and Leo IV UFDs (36 stars). This is the first time that *all* abundances are derived under NLTE.

For each star, abundances of Na, Mg, Al, Si, Ca, Ti, Fe, Ni, Sr, and Ba were obtained, provided the corresponding lines could be measured. The NLTE effects on the derived abundances are found to be different in magnitude and sign, depending on the chemical species and atmospheric parameters.

The first major impact of a homogeneous set of atmospheric parameters combined with a NLTE treatment is a substantial reduction of the spread in abundance ratios at given metallicity compared to a simple compilation of the literature data. This influences the abundance trends as follows:

- Any discrepancy in the level of the [α/Fe] plateau between α-elements Mg, Ca, and Ti is now removed. It is valid for all galaxies and particularly visible for the most populated galaxies in our sample, i.e. Sculptor, Ursa Minor, and the MW halo.
- In the [α/Fe] versus metallicity diagrams, all classical dSphs, i.e. Sculptor, Ursa Minor, Sextans, and Fornax, scatter around the mean of the Milky Way halo stars, [α/Fe] $\simeq 0.3$; this suggests an enrichment of these galaxies by massive stars in numbers following classical IMF. Our results for the MW giants are fully consistent with the NLTE abundances derived for the MW halo dwarfs by Zhao et al. (2016).
- The most dramatic effect of NLTE is found for the Na/Al abundance ratios. The LTE analysis suggests a substantial overabundance of sodium relative to aluminum in all types of galaxies, at the level of [Na/Al] ~ 0.8, while [Na/Al] is reduced down to $\sim$0.2 in NLTE.
- For [Na/Fe], [Na/Mg], and [Al/Mg], the Milky Way and dSphs reveal indistinguishable trends with metallicity suggesting that the processes of Na and Al synthesis (carbon burning process) are identical in all systems, independent of their mass.
- The relation between Ni and Fe is extremely tight, much tighter than with any other element produced by SNeII.

The abundance trends deliver important clues to galaxy star formation histories. We can firmly assess the following impact of SNeIa ejecta on the chemical evolution of some of the faintest dwarfs known:

- The Boötes I UFD reveals a decline in α/Fe and possesses a low [α/Fe] population, with consistent evidence from the three elements for which data are available, i.e. Mg, Ca, and Ti. This can be a signature of the SNe Ia contribution to iron and a duration of about 1 Gyr for star formation in this galaxy.
- The low [α/Fe] value of the S1 star in the Leo IV UFD suggests that this galaxy had a long enough star formation history to be polluted by SNeIa ejecta.
- In contrast, Ursa Major II ($M_V = -4.2$), which is the faintest of our three UFDs (McConnachie 2012) and has three stars that cover the $-3 <$ [Fe/H] < -2.3 metallicity range, falls exactly on the [Mg/Fe] and [Ca/Fe] plateau formed by the MW halo stars, indicating the dominance of SNeII in its chemical evolution and a short formation timescale.

We provide further evidence that the mass of a galaxy is an important driver of its chemical evolution. We bring in constraints on nucleosynthesis sites, particularly for the neutron-capture elements, and on the mixing of the SN ejecta in the galaxy interstellar medium as follows:

- Inhomogeneous mixing and/or stochastic effects from small numbers of SNe II is robustly documented in the Sculptor dSph. One star, ET0381, is strongly deficient in all elements except for the Fe-group, possibly missing the ejecta of the most massive Type II supernovae (Jablonka et al. 2015). The star 11_1_4296 is Mg- and Ca-poor. The two [Fe/H] $\simeq -3$ stars, 002_06 and 074_02, show no signature of the Ba II 4934 Å resonance line in their spectra, suggesting substantially lower Ba abundance, by more than 1 dex, compared with that of the star 03_059, which has a similar metallicity. Neither Ba nor Sr can be measured in the two [Fe/H] $\simeq -3.7$ stars, 11_1_4296 and S1020549, while the Sr II and Ba II lines are reliably detected in two other stars with almost the same metallicity and even in the EMP star 07-50.
- The classical dSphs behave like the MW halo with respect to [Sr/Fe]: large dispersion below [Fe/H] ~ -3, but close-to-solar Sr/Fe ratio above this metallicity. None of the classical dSphs reach a solar Ba/Fe ratio. Magnesium seems to be a better tracer of the Sr evolution than iron. The [Sr/Mg] ratios are nearly flat in the $-4 \lesssim$ [Ba/H] $\lesssim -2.5$ range, unlike [Ba/Mg], which is substantially lower than [Sr/Mg] at [Ba/H] $\simeq -4$, but approaches [Sr/Mg] at the highest Ba abundances.
- The massive dSphs follow the Sr/Ba trends defined by the MW halo stars, either at subsolar value or along the declining [Sr/Ba] trend with increasing [Ba/H]. This suggests two different nucleosynthesis channels for Sr.
- The UFDs are depleted in Sr and Ba relative to Fe and Mg with very similar ratios of [Sr/Mg] $\simeq -1.3$ and [Ba/Mg] $\simeq -1$ on the entire range of metallicity (and Mg abundance) for Boötes I and UMa II. The only star available in Leo IV does not stand out with respect to [Sr/Mg], while its lower [Ba/Mg] ratio compared with that for the other two UFDs is probably related to the early dispersed mode of Ba production. Subsolar Sr/Ba ratios of the stars in Boötes I and UMa II may indicate a common origin of Sr and Ba in the classical main r-process, although the statistics of Sr/Ba measurements is poor. The fact that the faint galaxies miss the second channel of Sr production could be explained by an undersampling of the IMF, possibly at its high tail.

This study is the first step in our goal of carrying out further NLTE high-resolution studies of dSphs. We plan to increase the number and mass range of the galaxies explored and to extend the observed metallicity range of their populations.

Acknowledgements. We thank Judith G. Cohen, Rana Ezzeddine, Anna Frebel, and Joshua D. Simon for providing stellar spectra, David Yong for double checking the observed equivalent widths of the Ba II lines in the Boötes I stars. The authors are indebted to the International Space Science Institute (ISSI), Bern, Switzerland, for supporting and funding the international team "The Formation and Evolution of the Galactic Halo". L.M., Y.P., and T.S. acknowledge financial support from the grant on Leading Scientific Schools 9951.2016.2. We made use of the MARCS, SIMBAD, and VALD databases.

References

Alexeeva, S., Pakhomov, Y., & Mashonkina, L. 2014, Astron. Lett., 40, 406
Anders, E., & Grevesse, N. 1989, Geochim. Cosmochim. Acta, 53, 197
Andrievsky, S. M., Spite, M., Korotin, S. A., et al. 2007, A&A, 464, 1081

Andrievsky, S. M., Spite, M., Korotin, S. A., et al. 2008, A&A, 481, 481
Andrievsky, S. M., Spite, M., Korotin, S. A., et al. 2009, A&A, 494, 1083
Andrievsky, S. M., Spite, M., Korotin, S. A., et al. 2010, A&A, 509, A88
Andrievsky, S. M., Spite, F., Korotin, S. A., et al. 2011, A&A, 530, A105
Aoki, W., Beers, T. C., Honda, S., & Carollo, D. 2010, ApJ, 723, L201
Arlandini, C., Käppeler, F., Wisshak, K., et al. 1999, ApJ, 525, 886
Asplund, M. 2005, ARA&A, 43, 481
Barklem, P. S., Piskunov, N., & O'Mara, B. J. 2000, A&AS, 142, 467
Barklem, P. S., Christlieb, N., Beers, T. C., et al. 2005, A&A, 439, 129
Barklem, P. S., Belyaev, A. K., Dickinson, A. S., & Gadéa, F. X. 2010, A&A, 519, A20
Barklem, P. S., Belyaev, A. K., Spielfiedel, A., Guitou, M., & Feautrier, N. 2012, A&A, 541, A80
Baumueller, D., & Gehren, T. 1996, A&A, 307, 961
Baumueller, D., & Gehren, T. 1997, A&A, 325, 1088
Baumueller, D., Butler, K., & Gehren, T. 1998, A&A, 338, 637
Bautista, M. A., Gull, T. R., Ishibashi, K., Hartman, H., & Davidson, K. 2002, MNRAS, 331, 875
Becker, W., & Werth, G. 1983, Z. Phys. A Hadrons Nucl., 311, 41
Belyaev, A. K. 2013, A&A, 560, A60
Belyaev, A. K., Yakovleva, S. A., & Barklem, P. S. 2014, A&A, 572, A103
Belyaev, A. K., Yakovleva, S. A., Guitou, M., et al. 2016, A&A, 587, A114
Belyakova, E. V., & Mashonkina, L. I. 1997, Astron. Rep., 41, 530
Bergemann, M. 2011, MNRAS, 413, 2184
Bergemann, M., Hansen, C. J., Bautista, M., & Ruchti, G. 2012, A&A, 546, A90
Bisterzo, S., Travaglio, C., Gallino, R., Wiescher, M., & Käppeler, F. 2014, ApJ, 787, 10
Blatt, R., & Werth, G. 1982, Phys. Rev. A, 25, 1476
Bliss, J., Arcones, A., Montes, F., & Pereira, J. 2017, J. Phys. G Nucl. Phys., 44, 054003
Borghs, G., de Bisschop, P., van Hove, M., & Silverans, R. E. 1983, Hyperfine Interact., 15, 177
Brix, P., & Kopfermann, H. 1952, Landolt-Börnstein, I/5 (Berlin: Springer)
Butler, K., & Giddings, J. 1985, Newsletter on the analysis of astronomical spectra, No. 9 (University of London)
Christlieb, N., Beers, T. C., Barklem, P. S., et al. 2004, A&A, 428, 1027
Cohen, J. G., & Huang, W. 2010, ApJ, 719, 931
Cohen, J. G., Christlieb, N., Thompson, I., et al. 2013, ApJ, 778, 56
Drawin, H.-W. 1968, Z. Phys., 211, 404
Farouqi, K., Kratz, K.-L., Pfeiffer, B., et al. 2010, ApJ, 712, 1359
François, P., Depagne, E., Hill, V., et al. 2007, A&A, 476, 935
Frebel, A., Simon, J. D., Geha, M., & Willman, B. 2010, ApJ, 708, 560
Frebel, A., Norris, J. E., Gilmore, G., & Wyse, R. F. G. 2016, ApJ, 826, 110
Gehren, T., Liang, Y. C., Shi, J. R., Zhang, H. W., & Zhao, G. 2004, A&A, 413, 1045
Gilmore, G., Norris, J. E., Monaco, L., et al. 2013, ApJ, 763, 61
Grevesse, N., & Sauval, A. J. 1998, Space Sci. Rev., 85, 161
Grevesse, N., & Sauval, A. J. 1999, A&A, 347, 348
Gustafsson, B., Edvardsson, B., Eriksson, K., et al. 2008, A&A, 486, 951
Hansen, C. J., Bergemann, M., Cescutti, G., et al. 2013, A&A, 551, A57
Hayek, W., Wiesendahl, U., Christlieb, N., et al. 2009, A&A, 504, 511
Hill, V., Christlieb, N., Beers, T. C., et al. 2017, A&A, 607, A91
Honda, S., Aoki, W., Kajino, T., et al. 2004, ApJ, 607, 474
Idiart, T., & Thévenin, F. 2000, ApJ, 541, 207
Izutani, N., Umeda, H., & Tominaga, N. 2009, ApJ, 692, 1517
Jablonka, P., North, P., Mashonkina, L., et al. 2015, A&A, 583, A67
Ji, A. P., Frebel, A., Simon, J. D., & Chiti, A. 2016, ApJ, 830, 93
Kirby, E. N., & Cohen, J. G. 2012, AJ, 144, 168
Kobayashi, C., & Nomoto, K. 2009, ApJ, 707, 1466
Koposov, S. E., Gilmore, G., Walker, M. G., et al. 2011, ApJ, 736, 146
Kratz, K.-L., Farouqi, K., Pfeiffer, B., et al. 2007, ApJ, 662, 39
Kurucz, R. L. 2005, Mem. Soc. Astron. It. Suppl., 8, 14
Lawler, J. E., Wickliffe, M. E., den Hartog, E. A., & Sneden, C. 2001, ApJ, 563, 1075
Lodders, K., Plame, H., & Gail, H.-P. 2009, in Landolt-Börnstein – Group VI: Astronomy and Astrophysics, Numerical Data and Functional Relationships in Science and Technology, Vol. 4B: Solar System, ed. J. E. Trümper, 4.4., 44
Mashonkina, L. 2013, A&A, 550, A28
Mashonkina, L. 2014, in IAU Symp., 298, eds. S. Feltzing, G. Zhao, N. A. Walton, & P. Whitelock, 355
Mashonkina, L., & Gehren, T. 2000, A&A, 364, 249
Mashonkina, L., & Gehren, T. 2001, A&A, 376, 232
Mashonkina, L., Gehren, T., & Bikmaev, I. 1999, A&A, 343, 519
Mashonkina, L. I., Shimanskiĭ, V. V., & Sakhibullin, N. A. 2000, Astron. Rep., 44, 790
Mashonkina, L., Korn, A. J., & Przybilla, N. 2007, A&A, 461, 261
Mashonkina, L., Zhao, G., Gehren, T., et al. 2008, A&A, 478, 529
Mashonkina, L., Christlieb, N., Barklem, P. S., et al. 2010, A&A, 516, A46
Mashonkina, L., Gehren, T., Shi, J.-R., Korn, A. J., & Grupp, F. 2011, A&A, 528, A87
Mashonkina, L., Sitnova, T., & Pakhomov, Y. 2016, Astron. Lett., 42, 606
Mashonkina, L., Jablonka, P., Pakhomov, Y., Sitnova, T., & North, P. 2017, A&A, 604, A129 (Paper I)
McConnachie, A. W. 2012, ApJ, 144, 4
McWilliam, A. 1998, AJ, 115, 1640
Nishimura, N., Sawai, H., Takiwaki, T., Yamada, S., & Thielemann, F.-K. 2017, ApJ, 836, L21
Nomoto, K., Kobayashi, C., & Tominaga, N. 2013, ARA&A, 51, 457
Norris, J. E., Yong, D., Gilmore, G., & Wyse, R. F. G. 2010, ApJ, 711, 350
Okamoto, S., Arimoto, N., Yamada, Y., & Onodera, M. 2012, ApJ, 744, 96
Pignatari, M., Gallino, R., Meynet, G., et al. 2008, ApJ, 687, L95
Placco, V. M., Frebel, A., Beers, T. C., & Stancliffe, R. J. 2014, ApJ, 797, 21
Raassen, A. J. J., & Uylings, P. H. M. 1998, A&A, 340, 300
Raiteri, C. M., Busso, M., Picchio, G., Gallino, R., & Pulone, L. 1991, ApJ, 367, 228
Reetz, J. K. 1991, Diploma thesis, Universität München
Revaz, Y., & Jablonka, P. 2012, A&A, 538, A82
Roderick, T. A., Mackey, A. D., Jerjen, H., & Da Costa, G. S. 2016, MNRAS, 461, 3702
Roederer, I. U. 2009, AJ, 137, 272
Roederer, I. U. 2017, ApJ, 835, 23
Roederer, I. U., Mateo, M., Bailey III, J. I., et al. 2016, AJ, 151, 82
Romano, D., Bellazzini, M., Starkenburg, E., & Leaman, R. 2015, MNRAS, 446, 4220
Ryabchikova, T., Piskunov, N., Kurucz, R. L., et al. 2015, Phys. Scr., 90, 054005
Ryabchikova, T., Piskunov, N., Pakhomov, Y., et al. 2016, MNRAS, 456, 1221
Rybicki, G. B., & Hummer, D. G. 1991, A&A, 245, 171
Rybicki, G. B., & Hummer, D. G. 1992, A&A, 262, 209
Sakhibullin, N. A. 1983, Trudy Kazanskaia Gorodkoj Astronomicheskoj Observatorii, 48, 9
Shi, J. R., Gehren, T., Butler, K., Mashonkina, L. I., & Zhao, G. 2008, A&A, 486, 303
Shi, J. R., Gehren, T., Mashonkina, L., & Zhao, G. 2009, A&A, 503, 533
Shimanskaya, N. N., Mashonkina, L. I., & Sakhibullin, N. A. 2000, Astron. Rep., 44, 530
Silverans, R. E., Borghs, G., Dumont, G., & van den Cruyce, J. M. 1980, Z. Phys. A Hadrons Nucl. , 295, 311
Simon, J. D., Jacobson, H. R., Frebel, A., et al. 2015, ApJ, 802, 93
Siqueira Mello, C., Spite, M., Barbuy, B., et al. 2013, A&A, 550, A122
Sitnova, T. M. 2016, Astron. Lett., 42, 734
Sitnova, T. M., Mashonkina, L. I., & Ryabchikova, T. A. 2016, MNRAS, 461, 1000
Skúladóttir, Á., Tolstoy, E., Salvadori, S., et al. 2015, A&A, 574, A129
Smith, G. 1981, A&A, 103, 351
Sneden, C., Cowan, J. J., Lawler, J. E., et al. 2003, ApJ, 591, 936
Spite, M., Cayrel, R., Hill, V., et al. 2006, A&A, 455, 291
Spite, M., Andrievsky, S. M., Spite, F., et al. 2012, A&A, 541, A143
Starkenburg, E., Hill, V., Tolstoy, E., et al. 2013, A&A, 549, A88
Steenbock, W., & Holweger, H. 1984, A&A, 130, 319
Tafelmeyer, M., Jablonka, P., Hill, V., et al. 2010, A&A, 524, A58
Taubenberger, S., Benetti, S., Childress, M., et al. 2011, MNRAS, 412, 2735
Travaglio, C., Galli, D., Gallino, R., et al. 1999, ApJ, 521, 691
Truran, J. W., Cowan, J. J., Pilachowski, C. A., & Sneden, C. 2002, PASP, 114, 1293
Tsujimoto, T., & Shigeyama, T. 2014, A&A, 565, L5
Ural, U., Cescutti, G., Koch, A., et al. 2015, MNRAS, 449, 761
Venn, K. A., Irwin, M., Shetrone, M. D., et al. 2004, AJ, 128, 1177
Wanajo, S., Sekiguchi, Y., Nishimura, N., et al. 2014, ApJ, 789, L39
Webster, D., Bland-Hawthorn, J., & Sutherland, R. 2015, ApJ, 799, L21
Woosley, S. E., & Hoffman, R. D. 1992, ApJ, 395, 202
Zhao, G., & Gehren, T. 2000, A&A, 362, 1077
Zhao, G., Mashonkina, L., Yan, H. L., et al. 2016, ApJ, 833, 225